ANALYSIS OF $J/\Psi \to \omega\pi^0\pi^0$ at BESIII

by

Alperen YÜNCÜ

B.S., Physics, Boğaziçi Üniversitesi, 2012

Submitted to the Institute for Graduate Studies in
Science and Engineering in partial fulfillment of
the requirements for the degree of
Master of Science

Graduate Program in Physics

Boğaziçi University

2015

ACKNOWLEDGEMENTS

I would like to give my deep gratitude to Assoc. Prof. Veysi Erkcan ÖZCAN and Assoc. Prof. İsmail Ruhi UMAN for their support and immense efforts. I would like to thank Prof. Metin ARIK and Prof. Serkant Ali ÇETİN for never hesitating to help.

Also, I would like to thank my teammates, Engin EREN and Onur Buğra KOLCU, without their help it would have been very hard to carry on with this analysis. I would like to thank my friends, Serhat IŞTIN, Sarper BAYSAL and Seda Nur TAŞÇI for their patience and endless assistance.

Last but not least, special thanks to my family and Elvan TORUN for being always patient and supportive and for never leaving me alone.

ABSTRACT

ANALYSIS OF $J/\Psi \to \omega\pi^0\pi^0$ at BESIII

Using a sample of 1.3 billion J/ψ events collected with the BESIII detector at the BEPCII storage ring, the decay channel $J/\psi \to \omega\pi^0\pi^0$ has been studied. Two of the lightest tetraquark candidates, $f_0(500)$ (a.k.a. σ) and $f_0(980)$ have been searched for. A Dalitz Plot analysis has been performed and in additon to $f_0(500)$ (σ) and $f_0(980)$, $f_2(1270)$, $b_1(1325)$, $\rho(1450)$, and $f_2(2300)$ have been observed. The analysis and background study indicate that this channel is suitable for a detailed study of the resonances through a Partial Wave Analysis.

ÖZET

BESIII'te $J/\Psi \to \omega\pi^0\pi^0$ ANALİZİ

BEPCII depolama halkası üzerindeki BESIII algıcında toplanan 1.3 milyar J/ψ olayı kullanılmak suretiyle $J/\psi \to \omega\pi^0\pi^0$ kanalı incelenmiştir. En hafif kuark-dörtlüsü adaylarından olan $f_0(500)$ (σ) ve $f_0(980)$ parçacıkları araştırılmıştır. Dalitz Plot analizi yapılmış olup $f_0(500)$ (σ) ve $f_0(980)$'in yanı sıra $f_2(1270)$, $b_1(1325)$, $\rho(1450)$ ve $f_2(2300)$ rezonanslarına rastlanmıştır. Analiz ve ardalan sonuçları Kısmi Dalga Analizi uygulamak için uygun bir kanal olduğunu göstermektedir.

TABLE OF CONTENTS

LIST OF FIGURES

LIST OF TABLES

LIST OF ACRONYMS/ABBREVIATIONS

BEPCII	The Beijing Electron-Positron Collider
BESIII	The Beijing Spectrometer
BOSS	BESIII Offline Software System
DST	Data Summary Tape
MDC	Multilayer Drift Chamber
MUC	Muon Controller
NQM	Naive Quark Model
PID	Particle IDentification
PWA	Partial Wave Analysis
QCD	Quantum ChromoDynamics
RPC	Resistive Plate Counters
TOF	Time Of Flight system

1. INTRODUCTION

Quark model was proposed by Gell-Mann in 1956 [1]. In the following decades, many $q\bar{q}$ and qqq states were discovered. Gell-Mann's Naive Quark Model (NQM) has been succesful to describe most hadronic states, especially for heavy hadrons [2]. However, for the light meson spectroscopy the situation is quite different [3]. Since the coupling of QCD becomes larger, the high order diagrams can not be neglected; and non-perturbative effects, which cannot be described within the NQM, blemish the NQM. Other models, guided by quantum chromo dynamics (QCD) or by QCD sum rules or QCD on a lattice, predict non-$q\bar{q}$ states such as: glueballs, hybrids, multiquarks, meson molecules... [4].

Multiquark states was first proposed by Jaffe in 1977 [5]. The hypothetical nonet of light scalar tetraquarks formed by σ, $K_0^*(800)$, $a_0(980)$ and $f_0(980)$ is poorly understood. Compared to expectation, all nine states are rather light and their mass ordering is inverted [6]. Moreover, this scalar nonet is often understood as effected Higgs nonet of strong interaction and σ is often referred to as the "Higgs boson of strong interaction" of which constituents are quarks [7, 8].

The search for multiquarks is a hot research topic. Indeed, recently two new multiquark candidates have been discovered: a pentaquark in LHCb and a tetraquark in BESIII [9, 10]. In BESII experiment in 2006, σ anf $f_0(980)$ are observed in $J/\psi \to \omega\pi^+\pi^-$ decay channel. In this study, the feasibility of using the $J/\psi \to \omega\pi^0\pi^0$ process, which involves multiple neutral final-state particles as opposed to the easily reconstructed $\omega\pi^+\pi^-$ channel, for a similar analysis is studied. Whether σ and/or $f_0(980)$ exist as intermediate resonance in the process of $J/\psi \to \omega\pi^0\pi^0$ is also investigated.

2. THEORY

2.1. Standard Model

Since the beginning of history, it has been always asked by men what are the building blocks of matter. In 1961, Sheldon Glashow proposed a way to combine electromagnetic and weak interactions, which is consdered as the first step to Standard Model [11]. Afterwards in 1967, Steven Weinberg and Abdus Salam have consolidated the Higgs mechanism into electroweak theory of Glashow and modern Standard Model formed [12–14]. The particles in the Standard Model are listed in Table 2.1, Table 2.2 and Table 2.3.

Table 2.1. List of quarks in the SM [15].

Generation	Particle	Anti-Particle	Charge	Mass	Isospin
1^{st} gen.	d	$\bar{d}$	$+2/3$	$2.3^{+0.7}_{-0.5}\,\mathrm{MeV}$	$1/2$
	u	$\bar{u}$	$-1/3$	$4.8^{+0.5}_{-0.3}\,\mathrm{MeV}$	$1/2$
2^{nd} gen.	s	$\bar{s}$	$+2/3$	$95 \pm 5\,\mathrm{MeV}$	0
	c	$\bar{c}$	$-1/3$	$1.275 \pm 0.025\,\mathrm{GeV}$	0
3^{rd} gen.	b	$\bar{b}$	$+2/3$	$4.18 \pm 0.03\,\mathrm{GeV}(\overline{\mathrm{MS}})$	0
	t	$\bar{t}$	$-1/3$	$173.21 \pm 0.51 \pm 0.71\,\mathrm{GeV}$	0

Table 2.2. List of leptons in the SM [15].

Generation	Particle	Anti-Particle	Charge	Mass
1^{st} gen.	e^-	e^+	-1	$0.511\,\mathrm{MeV}$
	ν_e	$\bar{\nu_e}$	0	$< 2\,\mathrm{eV}$
2^{nd} gen.	μ^-	μ^+	-1	$105.6\,\mathrm{MeV}$
	ν_μ	$\bar{\nu_\mu}$	0	$< 0.19\,\mathrm{MeV}$
3^{rd} gen.	τ^-	τ^+	-1	$1.777\,\mathrm{GeV}$
	ν_τ	$\bar{\nu_\tau}$	0	$< 18.2\,\mathrm{MeV}$

The structure of the Standard Model is the unitary group of $SU(3)\times SU(2)\times U(1)$,

Table 2.3. List of bosons in the SM [15].

Generation	Particle	Interaction	Spin	Charge	Mass
Gauge Bosons	γ	Electromagnetism	1	0	$< 10^{-18}\,\text{eV}$
	g	Strong Interaction	1	0	0
	Z^0	Weak Interaction	1	0	$80.385 \pm 0.015\,\text{GeV}$
	$W^{\pm}$	Weak Interaction	1	± 1	$91.1876 \pm 0.0021\,\text{GeV}$
Scalar Bosons	H^0	Higgs Mechanism & Yukawa couplings	0	0	$125.7 \pm 0.4\,\text{GeV}$

where $SU(3)$ and $SU(2) \times U(1)$ -Special Unitary groups- are used to develop multiplets interacting via strong and electroweak force, respectively.

2.2. QCD

Quantum Chromodynamics (QCD) is the theory of strong interaction, which describes the interaction of quarks and gluons to form hadrons. It has a group structure of $SU(3)$ of 3-color quarks and gluons. Thus, QCD Lagrangian is:

$$\mathcal{L}_{\text{QCD}} = \mathcal{L}_q + \mathcal{L}_g = \overline{\psi}_i (i(\gamma^\mu D_\mu)_{ij} - m\delta_{ij})\psi_j - \frac{1}{4} G^a_{\mu\nu} G^{\mu\nu}_a$$

where $\psi_i(x)$ is the quark field in the fundamental representation of the $SU(3)$ gauge group, D_μ is covariant derivative associated with local $SU(2)$ and $G^a_{\mu\nu}$ represents the gauge invariant gluon field strength tensor: [16]

$$D_\mu = \partial_\mu - igA^i_\mu \frac{\sigma^i}{2}$$
$$G^a_{\mu\nu} = \partial_\mu A^a_\nu + g\epsilon^{abc} A^b_\mu A^c_\nu$$

where $A^a_\mu(x)$ are the gluon fields in the adjoint representation of the $SU(3)$ gauge group.

Hadrons must be color singlet due to the color confinement. Thus, in $SU(3)$ symmetry, out of 3 flavors and 3 quarks $3 \bigotimes 3 \bigotimes 3 = 10 \bigoplus 8 \bigoplus 8 \bigoplus 1$ baryons can be

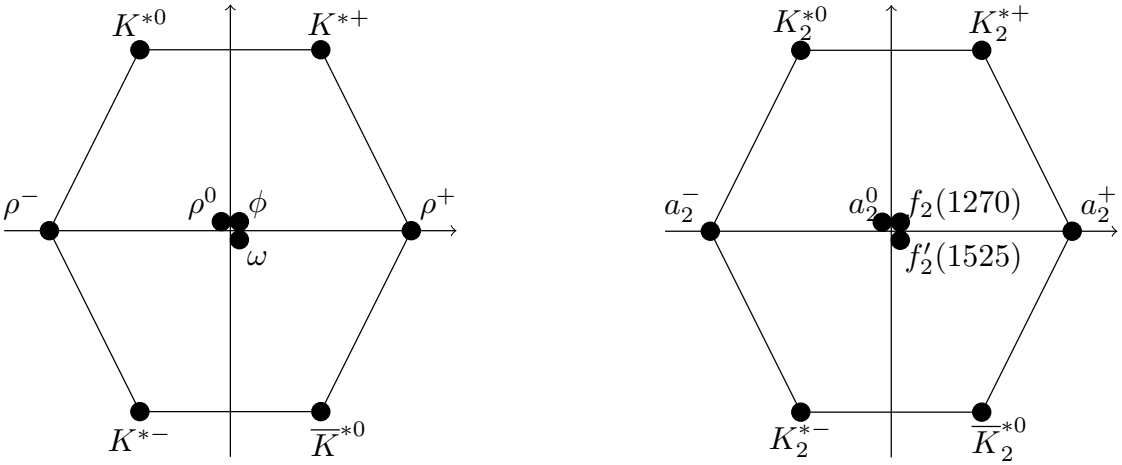

(a) 1^{--} Nonet. (b) 2^{++} Nonet.

Figure 2.1. Ground state vector and tensor meson nonets.

formed, while for mesons $3 \bigotimes \bar{3} = 8 \bigoplus 1$ states exists. Thus, for mesons there is an octet and a singlet, that is a nonet.

For mesons, The total spin (S) couples with orbital angular momentum (L) with a resulting total angular momentum (J). A fermion and antifermion have opposite parities so that P-parity equals $P = (-1)^{L+1}$ and C-parity equals $C = (-1)^{L+S}$. For every possible quantum number combination there exist a corresponding nonet. These combinations can be represented via "J^{PC}" notation. $J^{PC} = 1^{--}$ and $J^{PC} = 2^{++}$, respectively, corresponds to well-established vector and tensor meson nonets, shown at Figure 2.2. Meson's quantum numbers are also indicated using the spectroscopic notation $n^{2S+1}L_J$, where n is the principle quantum number and for $L = 0, 1, 2, 3, 4...$, traditionally, the letters $S, P, D, F, G...$ are used.

2.3. Exotic Bound States in QCD

While quark representation of the ground state of pseudoscalar (0^{-+}), vector (1^{--}) and tensor (2^{++}) nonets are well-established, the one relative to the ground

state of scalar nonet (0^{++}) is still controversial. This is due to the fact that there are too many possible candidates in the mass region up to 1.7 GeV: $f_0(500)$(or σ), $f_0(980)$, $f_0(1370)$, $f_0(1500)$, $f_0(1710)$ for isospin $I = 0$; $a_0(980)$, $a_0(1450)$ for isospin $I = 1$ and $K^*(800)$, $K_0^*(1430)$ for isospin $I = 1/2$.

This can be explained with the prediction that according to QCD, beside baryons (qqq) and mesons ($q\bar{q}$), there can be other bound states such as: glueballs, hybrids, multiquark states(tetraquark, pentaquark...etc) and meson molecules. Since gluons carry color charge they are interacting with each other as well as with quarks via strong interaction. Thus, they can form hybrid mesons($q\bar{q}g$) with quarks or glueball(ggg/gg). According to Weinstein and Isgur, a $q^2\bar{q}^2$ nonrelativistic potential model can be formulated using a four particle Schrödinger equation [17]. Also Jaffe proposed a four quark bag model in 1977 [5]. According to Jaffe's model, scalar mesons could be interpreted as tetraquark states ($q^2\bar{q}^2$). Also the mass degeneracy of $a_0(980)$ and $f_0(980)$, just below $K\bar{K}$ threshold and their decay to $K\bar{K}$ suggest to identify these states as bound $K\bar{K}$ systems. This model suggests two hypothetical configurations of lowest-lying scalar nonets, shown in Figure **??**. The $f_0(1500)$ does not fit these configurations and is considered the best candidate for a scalar glueball.

2.4. Exotic Bound States in $J/\psi \to \omega\pi\pi$

J/ψ is a $c\bar{c}$ meson with the quantum numbers 1^{--}. It is the first excited state of charmonium. Its name comes from Ting ($\overbrace{\rfloor}$), who was the leader for one of the two groups who discovered the particle [18], and by the fact that the reconstructed tracks of the process ($\psi' \to J/\psi\pi^+\pi^- \to \mu^+\mu^-\pi^+\pi^-$), in which J/ψ observed, have the shape of the letter ψ , the other group (Augustin and his group) suggested the name ψ [19]. An example of such a decay in BESIII is shown in Figure 2.3.

In the process $J/\psi \to \omega\pi^0\pi^0$, two possible reactions are possible according to

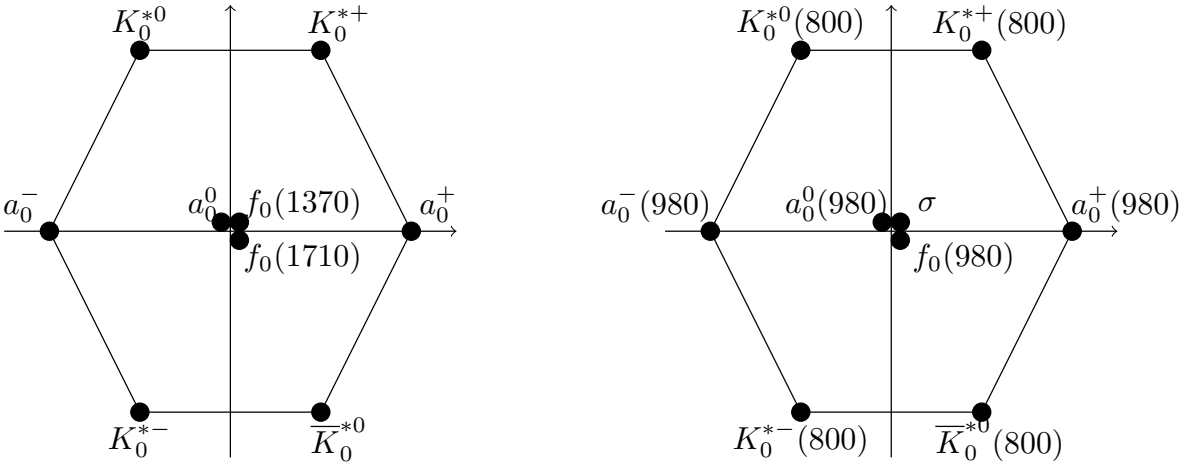

(a) $q\bar{q}$ Nonet. (b) $q^2\bar{q}^2$ Nonet.

Figure 2.2. Scalar Nonets(0^{++}).

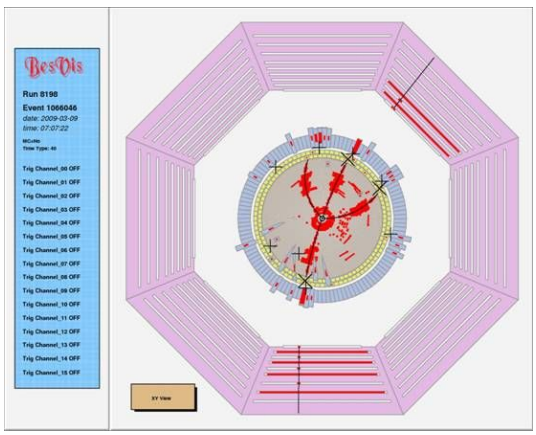

Figure 2.3. A reconstructed $\psi' \to \mu^+\mu^-\pi^+\pi^-$, through J/ψ, event at BESIII [20].

isobar model:

$$A : J/\psi \to \omega X, X \to \pi^0\pi^0$$

$$B : J/\psi \to Y\pi^0, Y \to \omega\pi^0$$

In addition, a direct producton without any resonance is possible, $J/\psi \to \omega\pi\pi$. The Feymann diagram for reaction type A is drawn in Figure 2.4. The channel is very

selective: because of selection rules only states with $J^{PC} = (\text{even})^{++}$ are possible for the isobar X. Also because of charge conservation only isospin 0 states are allowed. Possible resonances which can be investigated in the reaction A are therefore: $f_0(500)$ (σ), $f_0(980)$, $f_2(1270)$, $f_2(1565)$, $f_2(2300)$; in the reaction B: $b_1(1235)$ and $\rho(1450)$ for Y [21].

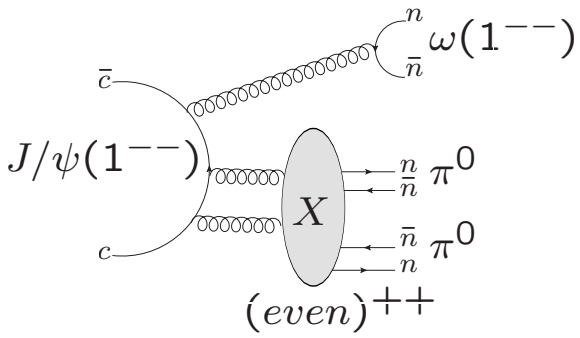

Figure 2.4. Feynmann diagram for $J/\psi \to \omega\pi^0\pi^0$.

$b_1(1235)$ is an axial vector(1^{+-}) and $\rho(1450)$ is a vector (1^{--}) meson. And both of them are $(d\bar{d} - u\bar{u})/\sqrt{2}$ ordinary mesons [15]. $f_2(1270)$ is a tensor meson from 2^{++} nonet and its quark content is $(u\bar{u} + d\bar{d})/\sqrt{(}2)$ [22]. And $f_2(2300)$ is an $s\bar{s}$ meson with quantum numbers 2^{++}. However, its not from a single nonet, it is a composite of 3 mesons: $s\bar{s}$ from $2\,^3\mathrm{P}_2$ 2^{++} nonet, $s\bar{s}$ from $1\,^3\mathrm{F}_2$ 2^{++} nonet, $s\bar{s}$ from $3\,^3\mathrm{P}_2$ 2^{++} nonet [23].

$f_0(980)$ is a composite particle. It includes mostly tetraquark [24] and small amount of glueball ($W_{\text{glueball}}[f_0(980)] \lesssim 15\%$) [25]. $f_0(980)$ can not be modelled as a Breit-Wigner resonance. Since its mass is very close to $K\bar{K}$ threshold, it should be modelled via the Flatté formalism [26]. Flatté formalism is a coupled channel analysis. To fit $f_0(980)$, the results of analysis for $\pi\pi$ and KK channel are needed. Thus, in this analysis the parameters fitted in the $J/\psi \to \omega\pi^+\pi^-$ and $J/\psi \to \omega K^+K^-$ are used for the g_{KK} term in the Flatté formula [21, 27].

$f_0(500)(\sigma)$ is the lightest tetraquark or meson molecule candidate [28]. Exotic mesons generally composite particles, a mixture of $q\bar{q}$ states, glueballs, meson-

molecules...etc; however, σ can be hardly interpreted a $q\bar{q}$ state or a glueball [25].

3. DETECTOR

3.1. Introduction

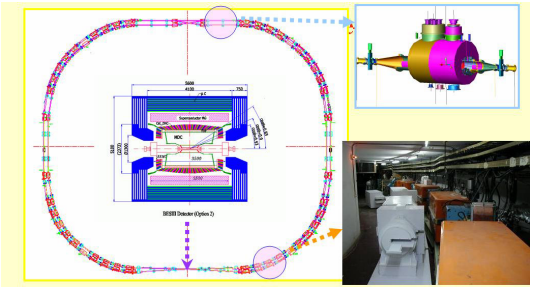

Figure 3.1. Schematic view of BEPCII and BESIII [29].

The BESIII Collaboration is an international collaboration that involves 31 universities from China, 13 from Europe, 5 from USA and 4 more from other Asian countries, which is hosted on BEPCII, a double-ring multi-bunch collider placed at IHEP, Beijing, People's Republic of China. The physics program of the BESIII experiment includes: [30]

- Tests of electroweak interactions with very high precision in both the quark and lepton sectors.
- High statistics studies of light hadron spectroscopy and decay properties.
- Studies on the production and decay properties of $J/\psi, \psi(2S)$ and $\psi(3770)$ states with large data samples and search for glueballs, quark-hybrids, multi-quark states and other exotic states via charmonium hadronic and radiative decays.
- Studies on τ-physics.
- Studies on charm physics, including the decay properties of D and D_s and charmed baryons.
- Precision measurements of QCD parameters and CKM parameters.
- Search for new physics by studying rare and forbidden decays, oscillations, and CP violations in *c-hadron* and τ-*lepton* sectors.

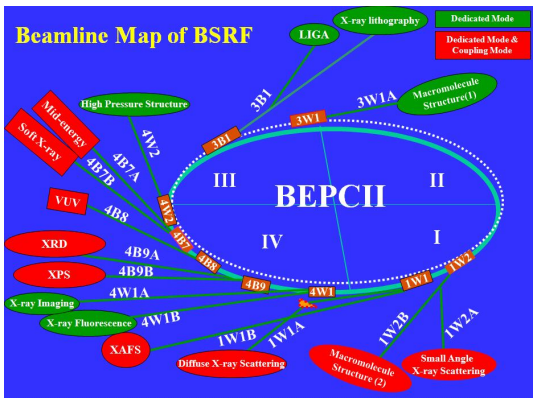

Figure 3.2. Schematic view of BEPCII [31].

3.2. BEPCII

The Beijing Electron-Positron Collider(BEPCII) is a double ring multi-bunch collider, with instantaneous luminosity of $10^{33}\,\mathrm{cm}^{-2}\,\mathrm{s}^{-1}$, optimized at a center of mass energy of $2\times1.89\,\mathrm{GeV}$. It has been in operation since 2008 and physics data taking started in March of 2009. It consists of a circular construction, 237.5 m in circumference. BEPCII is designed to collide e^+e^- beams in the energy range of $\sqrt{s} = (2-4.6)\,\mathrm{GeV}$. The design parameters of BEPCII are shown in Table 3.1 [32].

Table 3.1. The parameters of BEPCII [32].

Parameters	Values	Parameters	Values
Center of mass energy (GeV)	2-4.6	Beam current (A)	2×0.91
Circumference (m)	237.5	Bunch spacing (m/ns)	2.4/8
Number of rings	2	Bunch length ($\sigma_z; cm$)	1.5
RF frequency f_{rf} (MHz)	499.8	Bunch width ($\sigma_x; \mu m$)	~ 380
Peak luminosity at $2\times1.89\,\mathrm{GeV}(cm^{-2}s^{-1})$	10^{33}	Bunch height ($\sigma_y; \mu m$)	~ 5.7
		Relative energy spread	5×10^{-4}
Number of bunches	2×93	Crossing angle (mrad)	±11

3.3. BESIII

BEjing Spectrometer III(BESIII) detector placed inside the 1 T superconducting solenoid magnet (SSM) with a mean radius of 1.482 m and length of 3.52 m. It is intended to take advantage of the high luminosity provided by BEPCII, and to collect large data samples to accomplish the presented physics program. The expected data samples of each year of the BESIII are summarized in Table 3.2. BESIII utilizes a cartesian coordinate system with the z-axis defined along the beam direction, x-axis pointing towards the center of the BEPCII ring and y-axis pointing upwards [30].

Table 3.2. Expected BESIII data samples in a year [32].

States	Energy (GeV)	Peak luminosity ($10^{33}\,\mathrm{cm}^2\,\mathrm{s}^{-1}$)	Physics cross-section (nb)	Events/year
J/ψ	3.097	0.6	3400	1×10^{10}
$\psi(2S)$	3.686	1.0	640	3×10^9
$\tau^+\tau^-$	3.670	1.0	2.4	1.2×10^7
$D^0\bar{D}^0$	3.770	1.0	3.6	1.8×10^6
D^+D^-	3.770	1.0	2.8	1.4×10^6
D_sD_s	4.010	0.6	0.3	0.9×10^6
D_sD_s	4.170	0.6	0.9	2.7×10^6

Figure 3.3 shows the configuration of BESIII and identifies the main spectrometer components. The multilayer drift chamber(MDC) surrounds the beam pipe. Two superconducting quadrupoles (SCQs) are inserted in the conical shaped MDC endcaps as close as possible to the interaction point. The time-of-flight (TOF) system, consisting of two layers of plastic scintillator counters, is located on the outside of the main drift chamber. The CsI(Tl) electromagnetic calorimeter(EMC) is placed outside of the TOF system and inside the SSM. The muon identifier(MU) consists of layers of resistive plate chambers (RPCs) inserted in the gaps between steel plates of the flux return yoke. The polar angle coverage of the spectrometer is $21^\circ < \theta < 159^\circ$, which corresponds to a solid angle coverage of $\delta\Omega/4\pi = 0.93$. The main parameters of BESIII are summarized in Table 3.3.

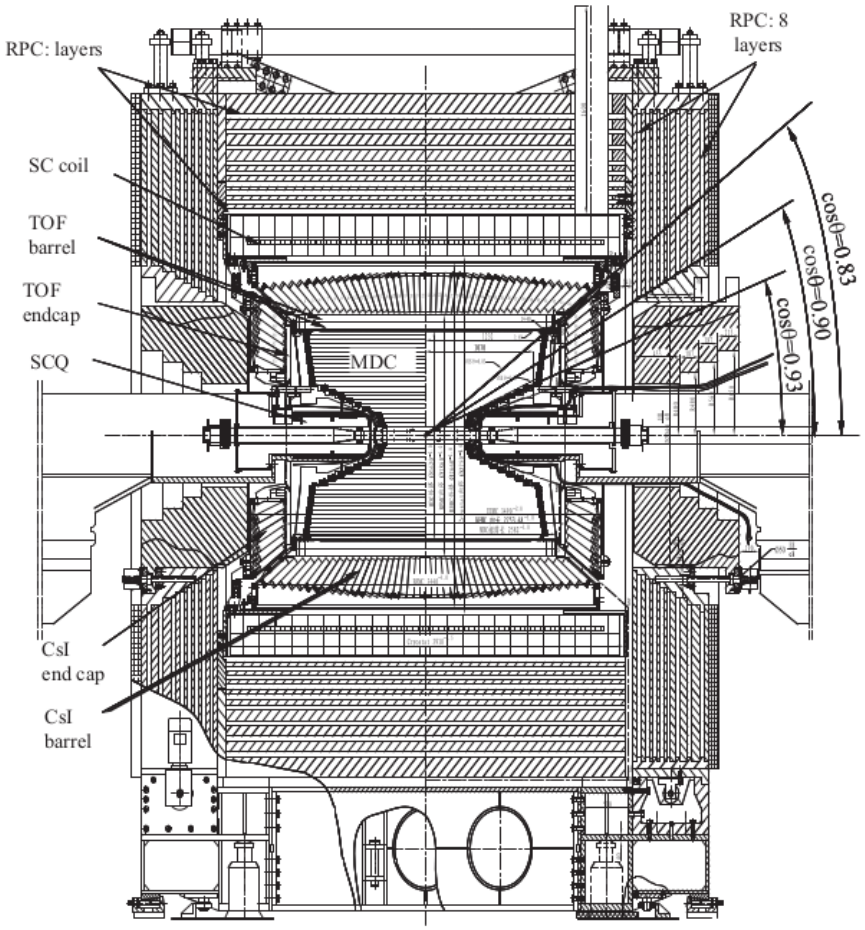

Figure 3.3. Schematic drawing of BESIII [32].

3.3.1. MDC

Multilayer Drift Chamber(MDC) is designed to reconstruct charged tracks(in 3D) including long lifetime hadrons(K^0_S, Λ), to determine the momenta of charged particles with excellent momentum resolution and good dE/dx measurement capability, to provide extrapolated track positions to outer components and to eliminate background tracks via level 1 trigger.

MDC is the innermost component of the detector, it has an inner radius of 59 mm (just 2 mm above the beam line) which covers a polar angle of $|\cos\theta| < 0.93$, and an outer radius of 810 mm which covers a polar angle of $|\cos\theta| < 0.83$ and a maximum length of 2400 mm, as shown in Figure 3.3. Its mechanical structure is shown in Figure

Table 3.3. The detector parameters of BESIII [32].

Subdetector	parameter	BESIII
MDC	Single wire $\sigma_{r\phi}$	130 μm
	σ_p/p (1 GeV/c)	0.5 %
	σ (dE/dx)	6 %
EMC	σ_E/E (1 GeV)	2.5 %
	position resolution (1 GeV)	0.6 cm
TOF	Barrel σ_T ps	100 ps
	End cup σ_T (ps)	110
MUON	the number of layers (Barrel/End cup)	9/8
	Cut-off momentum	0.4 MeV/c
Solenoid Magnet Field		1.0 T
$\delta\Omega/4\pi$		93 %

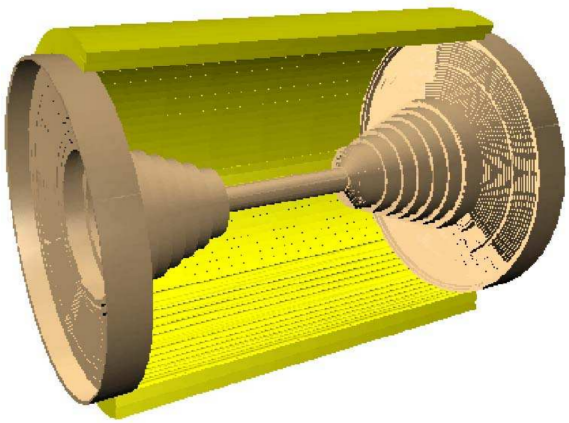

Figure 3.4. An overview of BESIII Main Drift Chamber [30].

3.5 and 3-D drawing is shown in Figure 3.4.

It consists of two chambers with no separator walls (since that would cause multiple scatterings) and they share the same gas volume(4 m^3) which is filled with a helium based gas mixture(He-C_3H_8, 40:60) at a pressure of 3 mbar. MDC has 43 cylindrical layers of drift cells which are placed coaxially with the beam pipe, 8 in the inner chamber and 35 in the outer chamber. All 8 layers in the inner chamber and 16 layers

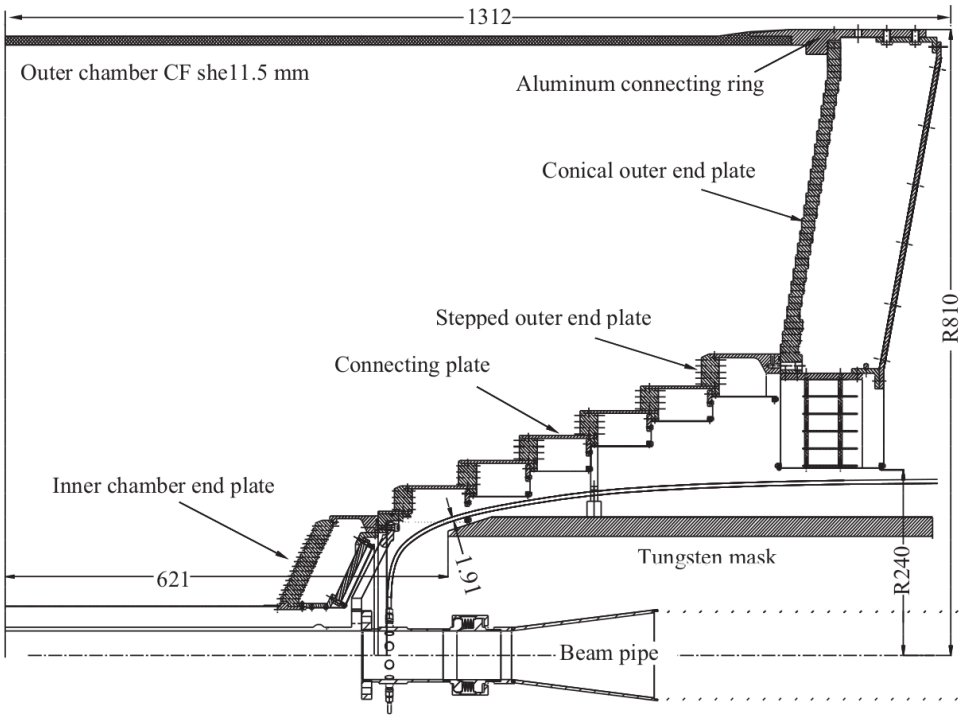

Figure 3.5. The MDC mechanical structure [32].

in outer chamber are stereo and the other 19 layers in outer chamber are axial. The geometric parameters of wire layers are shown at Table 3.4

Table 3.4. Geometric parameters of wire layers [32].

Layer No.	Superlayer No.	Tilted angle
1-4	1	U : $-$(3.0°- 3.3°)
5-8	2	V : +(3.4°- 3.9°)
9-20	3-5	A : 0°
21-24	6	U : $-$(2.4°- 2.8°)
25-28	7	V : +(2.8°- 3.1°)
29-32	8	U : $-$(3.1°- 3.4°)
33-36	9	V : +(3.4°- 3.6°)
37-43	10-11	A : 0°

3.3.1.1. Momentum Resolution. A simple model can be used to estimate the transverse momentum resolution, σ_{p_t}, in a multilayer tracking chamber with equally spaced

wire layers along the particle trajectories in a uniform axial magnetic field; which can be expressed as:

$$\frac{\sigma_{p_t}}{p_t} = \sqrt{\left(\frac{\sigma_{p_t}^{\text{wire}}}{p_t}\right)^2 + \left(\frac{\sigma_{p_t}^{\text{ms}}}{p_t}\right)^2}$$

where p_t is the transverse momentum of particles, $\sigma_{p_t}^{\text{wire}}$ is the momentum resolution resulting from the uncertainties of position measurements of individual wires and $\sigma_{p_t}^{\text{ms}}$ is the momentum resolution contribution due to multiple scatterings of tracks inside the tracking chamber. The momentum resolution of the MDC is better than 0.5% at $p_t = 1\,\text{GeV/c}$.

3.3.1.2. dE/dx Performance. The most probable value of the number of primary ionization pairs per centimeter is about 50 for the minimum ionizing particle tracks. And dE/dx resolution of the MDC is about 6% allowing $3\,\sigma$ π/K separation up to momenta of $\sim$ 770MeV/c [32] [30].

3.3.2. TOF

The TOF system, shown in Figure 3.6 is basically an array of plastic scintillation counters to measure the relative arrival times of particles, which is crucial for particle identification. There are 88 scintillation counters(Bicron 408 scintillator of 2300 mm length and with a trapeziodal cross section) in each two layers of Barrel array and 48 fan shaped scintillators (Bicron 404) on end cap arrays. Figure 3.6 shows the barrel TOF counters mounted on the outside of the MDC prior to the installation into the electromagnetic calorimeter. The inner and outer layers of the barrel have radii of 0.81 m and 0.86 m respectively, and the barrel covers a polar angle of $|\cos\theta| < 0.83$. It has been confirmed that the intrinsic time resolution with one TOF layer is less than 90 ps, for 1 GeV/c muons [32].

Figure 3.6. Two layers of barrel TOF counters taped to the outside of the MDC prior to the insertion into the electromagnetic calorimeter. The radius of the TOF counters is 870 mm [33].

3.3.2.1. Time Resolution. Time resolution, σ, can be expressed as:

$$\sigma = \sqrt{\sigma_i^2 + \sigma_b^2 + \sigma_l^2 + \sigma_z^2 + \sigma_e^2 + \sigma_t^2 + \sigma_w^2}$$

where σ_i is the intrinsic time resolution of the scintillation process, σ_b is the uncertainty of registering the global timing marker(accelerator RF clock) in the readout electronics, σ_l is the uncertainties in determining the interaction vertices when two beam bunches of 1.5 cm collide, σ_z is the uncertainty of hit positions along the scintillator bar, σ_e is the time resolution of the readout electronics, σ_t is the uncertainty of determining the particle flight time based on measuring flight path length and momentum, and σ_w is the uncertainty caused by the time walk in a fixed threshold discriminator due to signal amplitude fluctuations, given in Table 3.5 [32].

Table 3.5. Analysis of TOF time resolution for 1 GeV/c muon [32].

σ	Barrel(ps)	End cap(ps)
σ_i: counter intrinsic time resolution	80-90	80
σ_l: uncertainty from 15 mm bunch length	35	35
σ_b: uncertainty from clock system	~ 20	~ 20
σ_θ: uncertainty from θ-angle	25	50
σ_e: uncertainty from electronics	25	25
σ_t: uncertainty in expected flight time	30	30
σ_w: uncertainty from time walk	10	10
σ_1: total time resolution, one layer	100-110	110
σ_2: combined time resolution, two layers	80-90	-

3.3.2.2. Particle Identification. Including information from the MDC, TOF provides K/π separation over 95 % for the particles up to 0.9 GeV/c. K identification and misidentification rates can be seen in Figure 3.7 [32].

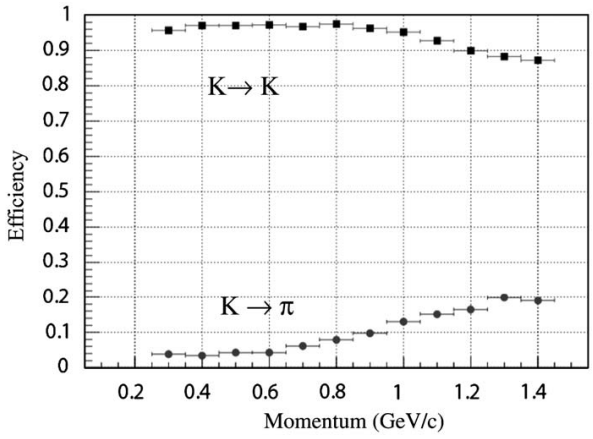

Figure 3.7. Efficiency of K identification and the rate of misidentification as π [32].

3.3.3. EMC

Electromagnetic Calorimeter (EMC) consists of 6272 CsI(TI) crystals placed on a barrel and two endcap sections, shown in Figure 3.8. The barrel section of EMC has an inner radius of 940 mm and a length of 2750 mm, and covers the polar angle of

$|\cos\theta| < 0.83$. The endcaps have inner radii of 500 mm and are placed at a distance of 1380 mm from the collision point, and covers the polar angle of $0.85 < |\cos\theta| < 0.93$. For mechanical support structures, there is a small gap of 50 mm between the barrel and endcaps. The total acceptance is 93% of 4π.

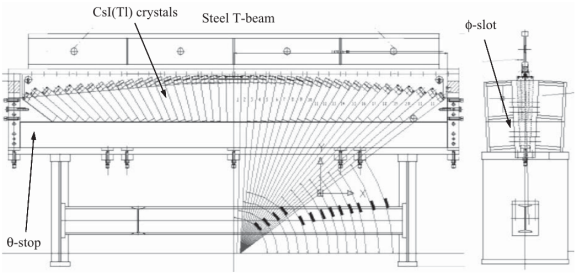

Figure 3.8. The side and cross-sectional views of the barrel super module assembly jig [32].

EMC is designed to measure the energy of electrons and photons from 20 MeV to 2 GeV, with an energy resolution of about $2.3\%/\sqrt{\mathrm{E(GeV)}} \oplus 1\%$. The design position resolution for an electromagnetic shower is $\sigma_{xy} \leq 6\,\mathrm{mm}/\sqrt{\mathrm{E(GeV)}}$ and the electronics noise for each crystal is less than 220 keV [30].

Table 3.6. Properties of thallium doped CsI(Tl) crystals [32].

Parameter	Values	Parameter	Vlaues
Radiation length X_0	1.85 cm	Signal decay time	680 ns (64%)
Moliere radius	3.8 cm		3.34 ms (36%)
Density	$4.53\,\mathrm{g/cm^3}$	temperature coefficient	$0.3\,\%/^{\circ}C$
Light yield	56000 γ's/Mev	dE/dx (per mip)	5.6 MeV/cm
Peak emission wavelength	560 nm	Hygroscopic sensitivity	Slight

3.3.4. Muon Identifier

Muon Identifier, shown in Figure 3.9, is the outermost part of the detector. It is constructed of Resistive Plate Counters (RPC) inserted in steel plates of magnetic flux return. The design and mechanical parameters of Muon Identifier is given in Table 3.7.

A gas mixture of $Ar/C_2F_4H_2/C_4H_{10}$ is used with the ratio 50 : 42 : 8 respectively for RPC system [32].

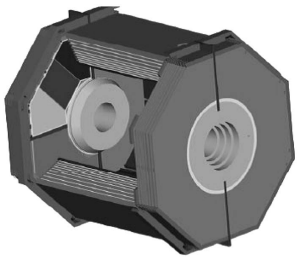

Figure 3.9. The 3D model of the BESIII muon identifier [32].

For each track, an Artificial Neural Network is used for muon/hadron identification. The input parameters are the maximum numbers of hit among layers the track penetrates, the depth of the track in the muon identifier, the match between the MUC(MUon Controller) stand-alone track and MDC track, the χ_2 of the MUC stand-alone track etc... The performance of identification is shown in Figure 3.10 [30].

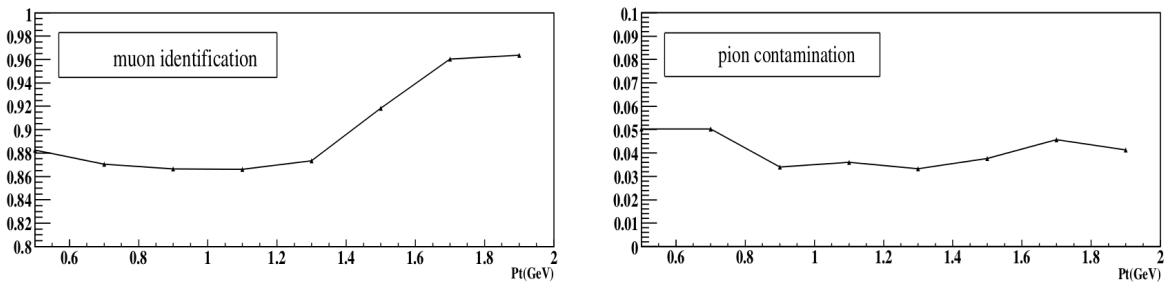

Figure 3.10. Muon identification and Pion contamination in identification process [30].

Table 3.7. Parameters of Muon Identifier [32].

Parameter		Value
$\Delta\Omega/4\pi$ (%)		89
Number of layers (Barrel/End caps)		9/8
Technology		RPC
Cut-off momentum (MeV/c)		400
Barrel	Inner radius (m)	1.700
	Outer radius (m)	2.620
	Length (m)	3.94
	Weight (ton)	300
	Steel plate thicknesses (cm)	$3, 3, 3, 4, 4, 8, 8, 8, 15$
	Gap between plates (cm)	4
	No. of RPC layers	9
	Polar angle coverage	$\cos\theta \leq 0.75$
End cap	Inner distance to IP (m)	2.050
	Outer distance to IP (m)	2.800
	Weight (ton)	4×52
	Steel plate thicknesses (cm)	$4, 4, 3, 3, 3, 5, 8, 8, 5$
	Gap between plates (cm)	4
	No. of RPC layers	8
	Polar angle coverage	$0.75 \leq \cos\theta \leq 0.89$

3.3.5. Trigger

The trigger, data acquisition and online computing systems are designed to accommodate multi-beam bunches separated by 8 ns and high data rate. There exist two levels of the trigger system, a hardware trigger (Level 1) and a software trigger (Level 3). At L1, the sub-detectors (TOF, MDC and EMC) produce sub-triggers for the global trigger logic. The entire system operates at 41.65 MHz synchronized with the accelerator RF system. With this trigger frequency, 3 beam crossings occur within every L1 clock cycle. The maximum L1 rate is about to be 4 kHz at 3.097 GeV. After L3, data rate written to permanent storage is about 3 kHz corresponding to 40 MB/s [32].

3.3.6. BESIII Offline Software System

BESIII Offline Software System (BOSS) is a complete collection of packages to process data and to perform physics analysis. It runs on the Scientific Linux and uses object oriented techniques in C++ programming language. BOSS consists of five functional parts: framework, simulation, reconstruction, calibration, and analysis tools.

The BOSS framework is based on the Gaudi package. And it uses utilities for event simulation, data processing and physics analysis; provided by Gaudi [34]. In BOSS, there are three types of data defined: raw data, reconstructed data and Data-Summary-Tape (DST) data. The DST data and the reconstructed data are in ROOT format. For simulation of BESSIII detector; a package based on the GEANT4 is used [35]. BOSS reconstruction package consists of a track-finding/track-fitting algorithm based on Kalman-Filter, to determine the momentum of charged particles, a particle identification (PID) algorithm, which is based on dE/dx and TOF measurements, a cluster-finding/shower-finding algorithm for EMC energy and position measurements and a muon track finder [30].

4. EVENT SELECTION

Since 2009, 1.3×10^9 J/ψ events have been collected by BESIII. A number of selection criteria are applied to these events in order to suppress the backgrounds and identify the signal events. In this section a brief summary of the collected and simulated events will be given, followed by a detailed list of event selection cuts.

4.1. Dataset

Data sets are processed via BOSS v6.6.4. For Monte-Carlo (MC) simulation samples GEANT-based simulation software BOOST is used [36]. The official inclusive MC samples of BESIII are used for background studies and decay modes are generated according to the current PDG values [15] by BesEvtGen [37].

4.2. Initial Event Selection

Final state of the signal has two charged particles, $\pi^{\pm}$, and 6 photons.

$$J/\psi \to \omega\pi^0\pi^0 \to \pi^+\pi^-\pi^0\pi^0\pi^0 \to \pi^+\pi^- 6\gamma$$

4.2.1. Charged Tracks

The selection criterion used for charged tracks is that there should be exactly 2 good charged particles with total charge of 0. The good particle is defined by requiring successful reconstruction of tracks and by limiting the maximum transverse and longitudinal distances to the interaction point, i.e. $r_{xy} \leq 1\,\text{cm}$ and $r_z \leq 5\,\text{cm}$.

4.2.2. Neutral Tracks

Since the final state of the signal has 6 photons, the number of photons has been set to exactly 6 good photons. The events with more than 6 photons are discarded due to the fact that the disadvantage of additional systematical errors overcomes the statistical gain.

The good photons are defined with parameters of its shower energy, shower time and seperation angle with charged tracks. The energy should be higher than 25 MeV for the barrel of the EMC ($|\cos\theta| < 0.8$) and higher than 50 MeV for the endcap of the EMC ($0.86 < |\cos\theta| < 0.92$). The different treshold energies are optimized to increase the signal to noise level. Because of the large Lorentz boost in the forward/backward direction the energy deposited by the photons in the endcaps is on average bigger than the one deposited in the barrel section of the EMC. The shower time should be in the interval of $[0, 14]$ (in units of 50 ns). The angle between the closest charged track and the shower should be $\geq 10°$. The results of photon selection are shown in Figure 4.1.

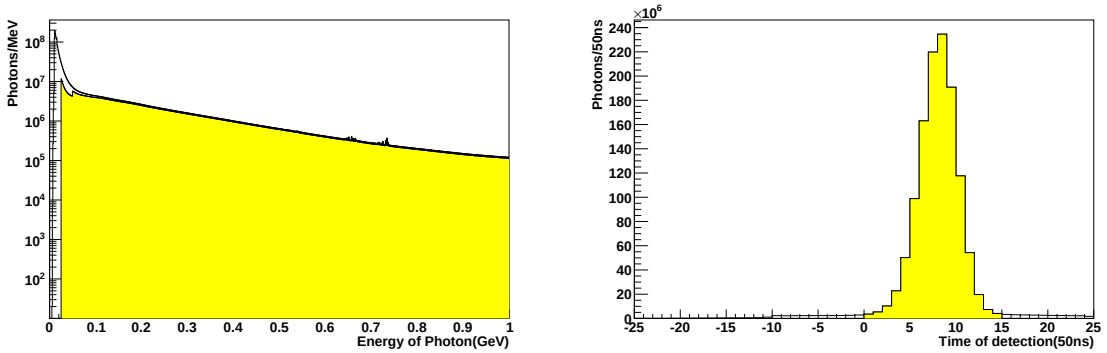

Figure 4.1. Good photon selection. The filled histograms depicked the photons satisfying the relevant criteria.

4.2.3. Particle Identification

To identify charged particles, the information provided by TOF and MUC are used. Charged particles other than π and K are eliminated easily and for π/K separation the standard π/K separation method of the BOSS system is used [30]. The result

of particle identification (PID) is shown at Figure 4.2.

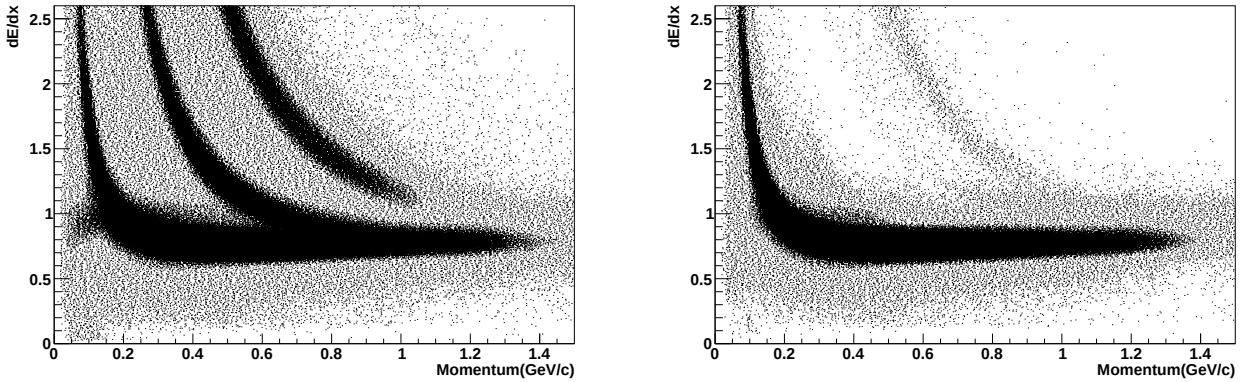

(a) dE/dx before PID.

(b) dE/dx after PID.

Figure 4.2. The effect of PID on dE/dx information.

4.3. Kinematic and Vertex Fits

Since there is no long-lived intermediate particle in the studied channel, vertex fit is applied for only the primary vertex. Instead of an exclusivity cut, to determine mother particle as J/ψ, 4C kinematic fit has been applied with components of the four momentum of J/ψ as constraints.

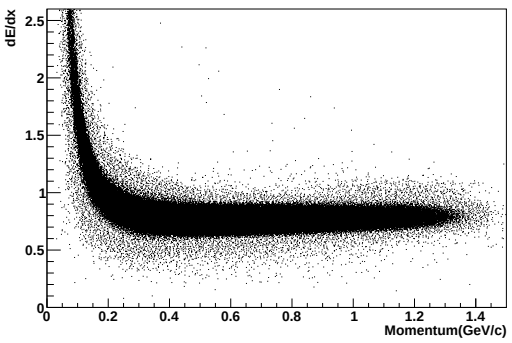

Figure 4.3. dE/dx information after fitting.

Another kinematic fit with 7 constraints, has been applied. For 7C-fit we use the 4 constraints of the previous kinematic fit and add another 3 constraints. 3 pairs of photons should come from 3 π^0's; however, contrary to J/ψ π^0's are not at rest so only their mass is considered as constraint. After vertex and 2 kinematic fits are applied, the events in which any of fits failed are rejected. The resulting cleaner dE/dx distribution is shown in Figure 4.3.

4.4. Final Event Selection

After preselection and fits, a cut on ω mass window has been used to determine events for $J/\psi \to \omega\pi^0\pi^0$, $\omega \to \pi^+\pi^-\pi^0$ over total invariant mass of $\pi^+\pi^-\pi^0$ as $|M_{\pi^+\pi^-\pi^0} - M_\omega| < 40\,\text{MeV}$ shown in Figure 4.4. Here M_ω is nominal mass from PDG [15].

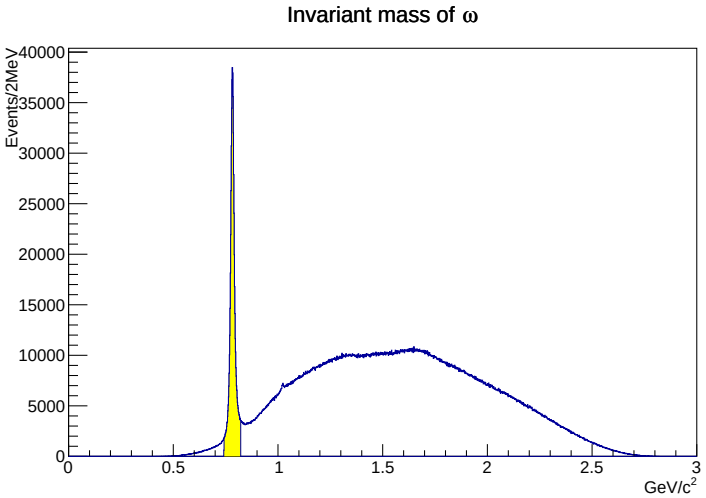

Figure 4.4. Invariant mass of $\pi^+\pi^-\pi^0$.

The criteria mentioned above are applied to an inclusive MC sample. As seen in Figure 4.5, the χ^2 of the 7C-fit for both signal and background peak around the same region; however, when normalized χ^2 is taken into account, the background is seen to have a flat component in addition to this peak and a maximum allowed value for the χ^2 is set as $\chi^2 < 60$.

This set of criteria is determined to eliminate background events and retain as

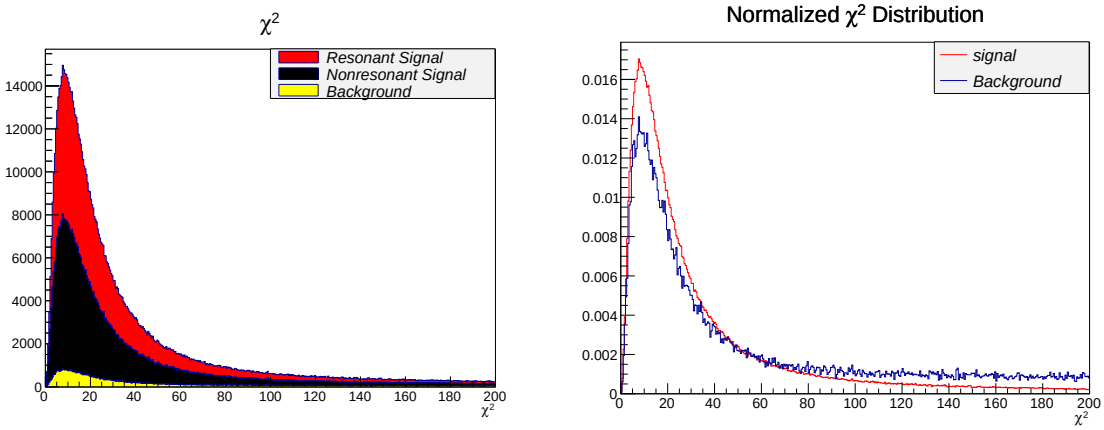

Figure 4.5. χ^2 distribution of inclusive MC sample.

many signal events, $J/\psi \to \omega\pi^0\pi^0$, as possible and the cutflow for both Signal and Data events is shown in Table 4.1.

Table 4.1. Selection list.

Cut	Real Data	Signal
Total Number of events	5.39×10^9	6.75×10^7
$N_{\text{charged particles}} = 2$	6.82×10^8	4.4×10^7
$N_{\text{photon}} = 6$	3.02×10^7	1.18×10^7
PID	2.06×10^7	1.12×10^7
Fitting(4C & vertex)	6.32×10^6	9.1×10^6
7C Fit	3.73×10^6	8.01×10^6
ω window	6.49×10^5	7.14×10^6
χ^2 cut	5.31×10^5	5.98×10^6

5. ANALYSIS

Mass distribution of $\pi^+\pi^-\pi^0$ is fit to the sum of a Voigt distribution (Breit-Wigner function convoluted with a Gaussian) to model the signal and a 2^{nd} order Chebyshev Polynomial modelling the background, as shown in Figure 5.1. The resulting parameters of the fit are: $m_\omega = 782.79 \pm 0.02\,\text{MeV}$, $\Gamma_\omega = 11.27 \pm 0.09\,\text{MeV}$, which agrees decently with the PDG values of $m_\omega = 782.65 \pm 0.12\,\text{MeV}$, $\Gamma_\omega = 8.49 \pm 0.08\,\text{MeV}$ [15]. According to the fit result, the background contamination in the selected data is 13.5%.

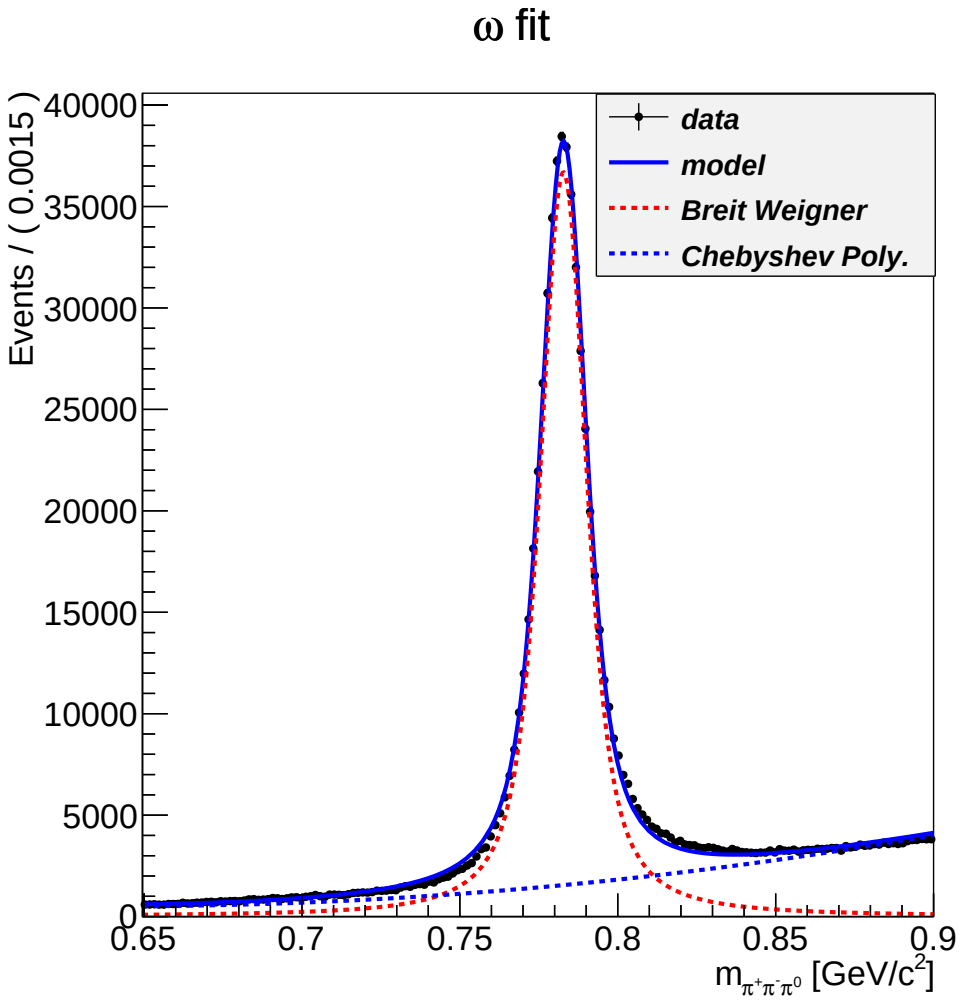

Figure 5.1. Fit to $m_{\pi\pi\pi}$ mass distribution.

5.1. Dalitz plot and its projections

After the event selection, the remaining sample is pure enough for studying the intermediate resonances in the $\omega\pi\pi$ system. For this, first a Dalitz plot analysis is performed. Dynamics of Dalitz Plot is explained in Appendix B. Since the final state particles are $\omega\pi^0\pi^0$, the Dalitz plot is a two-fold 2D histogram of $M^2_{\omega\pi}$ and $M^2_{\omega\pi}$. The Dalitz plot for exclusive MC without any intermediate resonances, shown in Figure 5.2, deviates from a flat distribution because of detector acceptance.

Figure 5.2. Dalitz Plot for exclusive MC.

The Dalitz plot of data, shown in Figure 5.3, the intermediate resonances are visible as vertical, horizontal and diagonal bands.

Projections of the Dalitz Plot are shown in Figure 5.4. The most easily spotted resonances that contribute to the distributions are shown with arrows. $b_1(1235)$

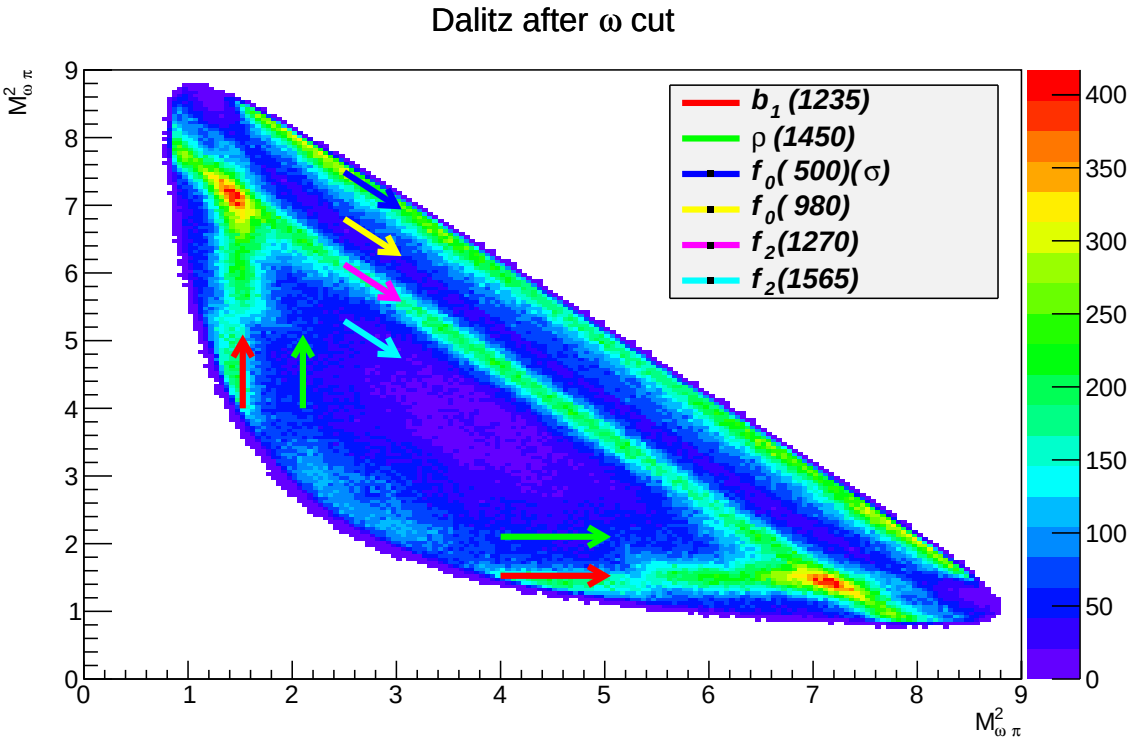

Figure 5.3. Dalitz Plot.

and $\rho(1450)$ contribute in the process $J/\psi \rightarrow \mathrm{Y}\pi^0$, $\mathrm{Y}\rightarrow \omega\pi^0$ and $f_0(500)$, $f_0(980)$, $f_2(1270)$and $f_2(1565)$ contribute in the process $J/\psi \rightarrow \mathrm{X}\omega$, $\mathrm{X}\rightarrow \pi^0\pi^0$.

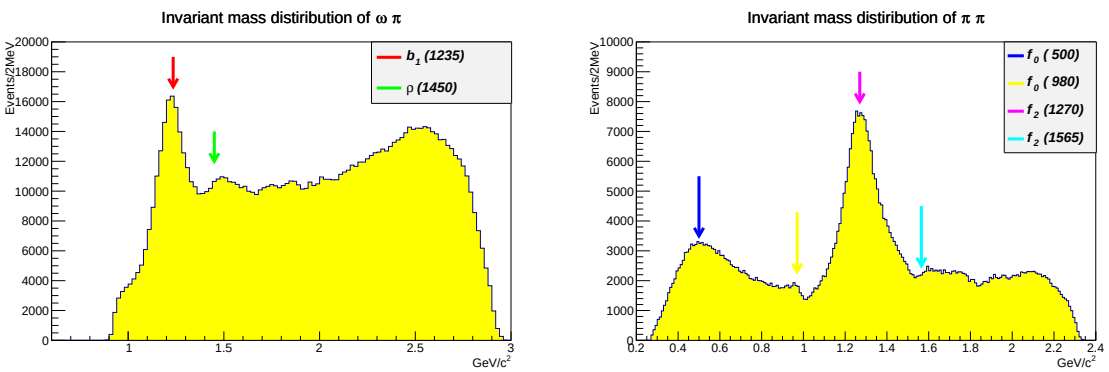

Figure 5.4. Projections of Dalitz Plot.

The results in the Dalitz plot and its projections can be compared to the earlier $J/\psi \rightarrow \omega\pi^+\pi^-$ results from BESII, shown in Figure 5.5. They appear to be in good agreement.

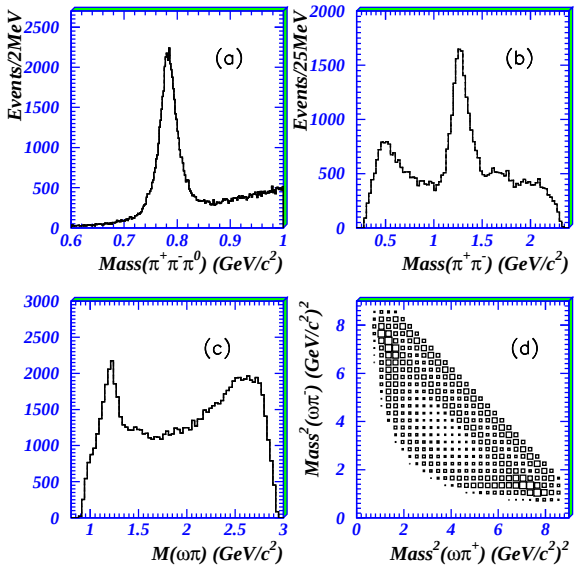

Figure 5.5. Results of a similar analysis ($J/\psi \to \omega\pi^+\pi^-$) from BESII [21].

5.2. Sidebin Analysis

To determine the shape of the background in the data, sidebins in the ω mass distribution are analyzed. Chosen sidebins have the same width as the ω mass window but their centers are shifted by $\pm 100\,\mathrm{MeV}$, as shown in Figure 5.6. The signal contribution is about 8% of the total number of events in the two sidebins, as determined by integrating the functions obtained through the $\omega-$mass fit.

Invariant mass distributions of $\omega\pi^0$ and $\pi^0\pi^0$ for the sidebins are shown in Figure 5.7.

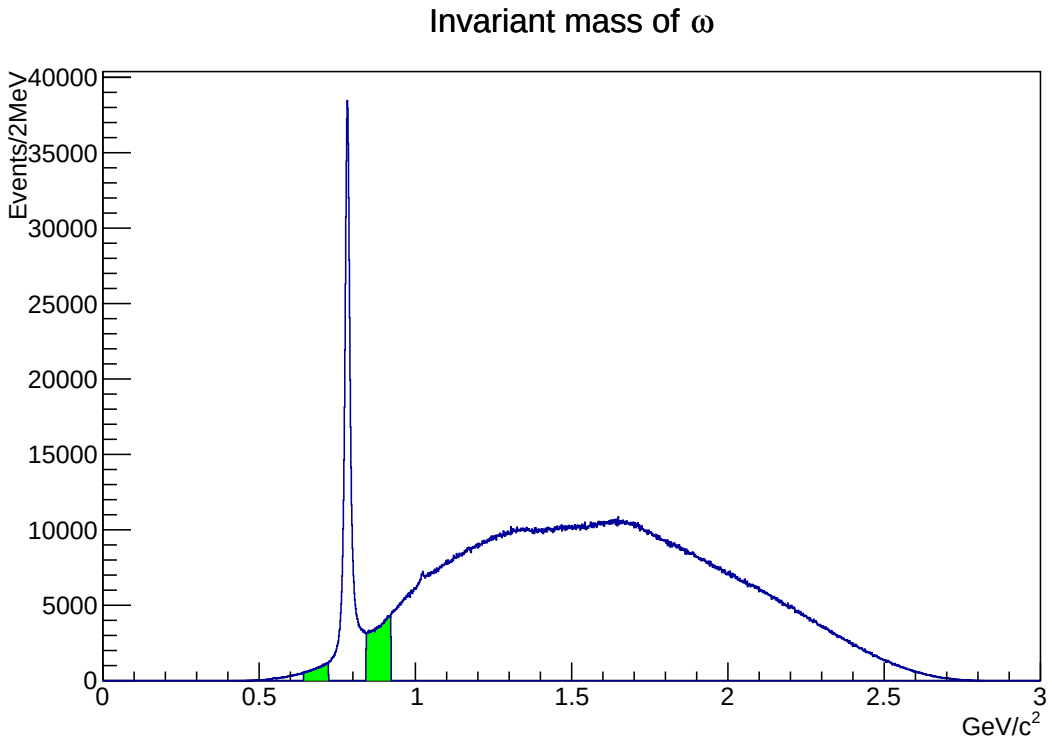

Figure 5.6. Sidebins in the ω mass distribution.

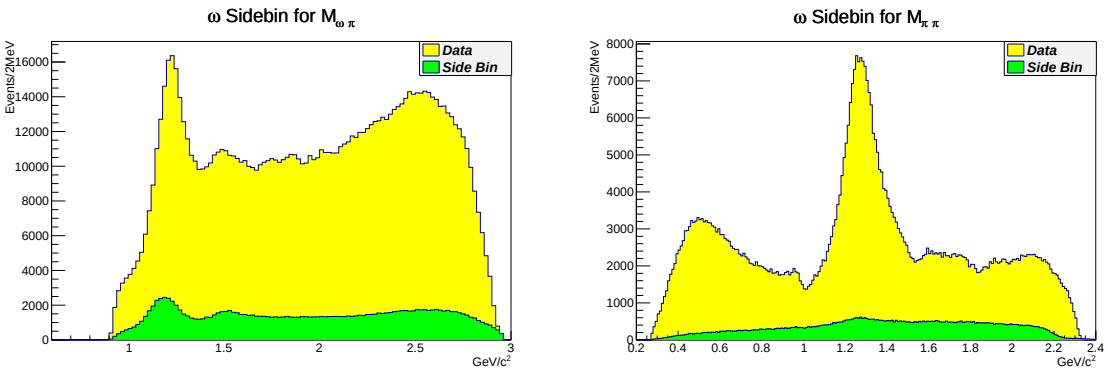

Figure 5.7. Mass distributions for the ω mass sidebins.

5.3. Partial Wave Analysis

Partial Wave Analysis (PWA) is widely used in high energy experimental physics. It is used for determining the widths, masses and spin parities of intermediate resonances via analyzing the correlation between momenta of final state particles. The basis of PWA is relativistic kinematics [30].

The helicity formalism is used in PWA. The general form of the decay amplitude for hadronic J/ψ decays is:

$$A = \psi_\mu(m) A^\mu = \psi_\mu(m) \sum_i \Lambda_i U_i^\mu$$

And for dynamical part relativistic Breit-Wigner function is used. Data are fitted using the unbinned log-likelihood method. For this purpose a sample of 67.5 million exclusive MC data has been produced. To take into account detector acceptance, the MC data has been submitted to the same selection criteria as the real data. The results of the fit are the masses, widths and coupling constants of the included resonances.

In the initial step, only dominant resonances ($b_1(1235)$ and $f_2(1270)$ are used to fit to the data. The mass distributions are shown in Figure 5.8 and the angular distributions are shown in Figure 5.9 and Figure 5.10, the crosses are real data, yellow histogram is the fit function and red histogram is sidebins.

This gives an absolut value of log-likelihood $\ln \mathcal{L} = 405818$.

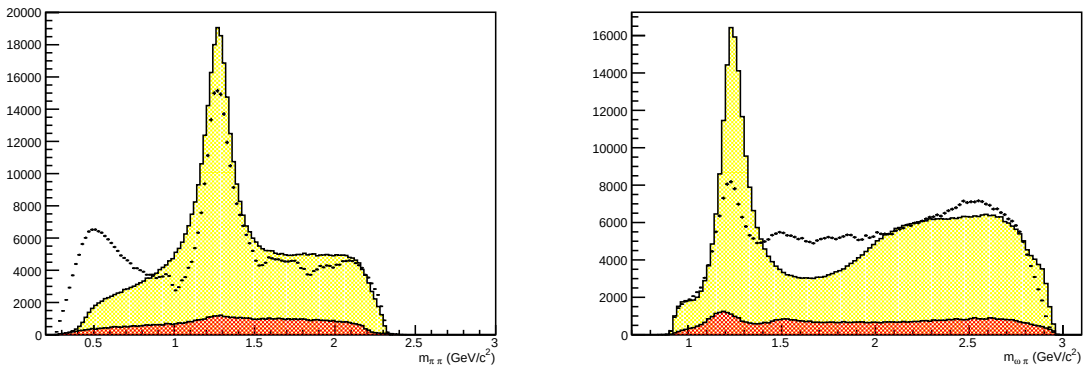

Figure 5.8. The invariant mass distuributions of PWA for $b_1(1235)$ and $f_2(1270)$. The left histogram is the invariant mass distribution of $\pi^0\pi_0$, the right histogram is the invariant mass distribution of $\omega\pi_0$.

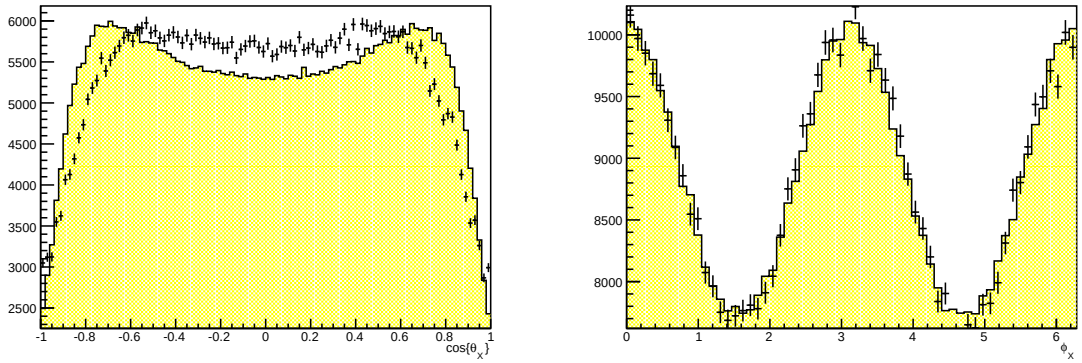

Figure 5.9. The production angular distributions of PWA for $b_1(1235)$ and $f_2(1270)$. The angular distributions of X in J/ψ rest frame for $J/\psi \to \omega X$ (the polar angle θ (left) and the azimuthal angle ϕ (right)).

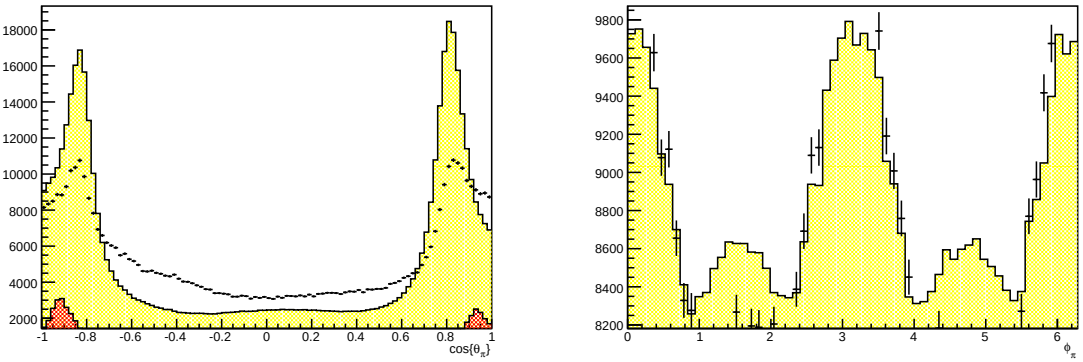

Figure 5.10. The decay angular distribution PWA for $b_1(1235)$ and $f_2(1270)$. The angular distribution of π^0 in X rest frame for $X \to \pi^0\pi^0$ (the polar angle θ (left) and the azimuthal angle ϕ (right)).

However, the fit of the mass distribution is not satisfactory. When σ and $f_0(980)$ are added to the PWA, the absolut value of log-likelihood decrease to $\ln \mathcal{L} = 204066$.

And the result is improved, as shown in Figure 5.11, Figure 5.12 and Figure 5.13, the crosses are real data, yellow histogram is the fit function and red histogram is sidebins.

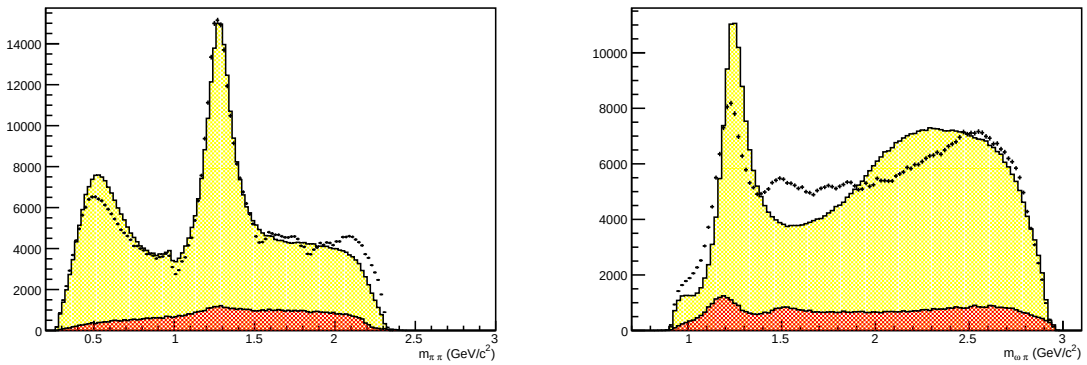

Figure 5.11. The invariant mass distuributions of pwa for $b_1(1235)$, $f_2(1270)$, σ and $f_0(980)$. the left histogram is the invariant mass distribution of $\pi^0\pi_0$, the right histogram is the invariant mass distribution of $\omega\pi_0$.

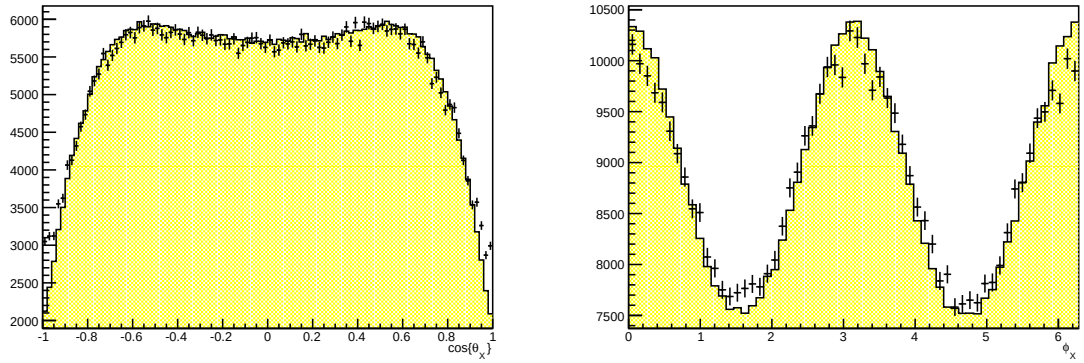

Figure 5.12. The production angular distributions of pwa for $b_1(1235)$, $f_2(1270)$, σ and $f_0(980)$. the angular distributions of x in j/ψ rest frame for $j/\psi \to \omega x$ (the polar angle θ (left) and the azimuthal angle ϕ (right)).

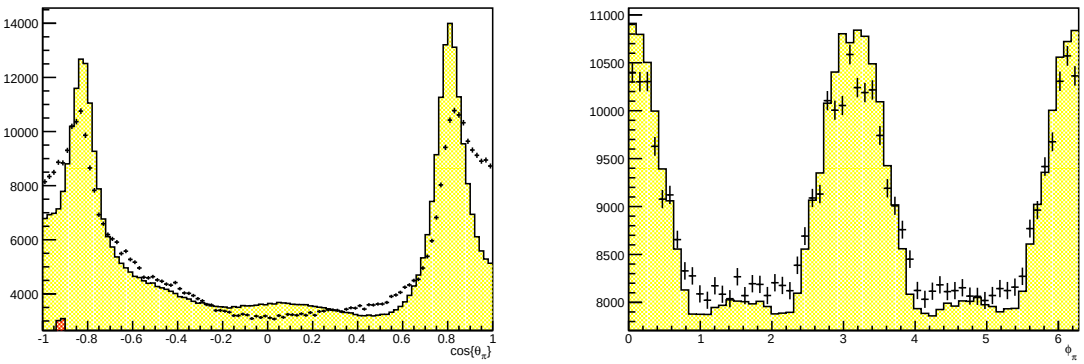

Figure 5.13. The decay angular distribution pwa for $b_1(1235)$, $f_2(1270)$, σ and $f_0(980)$. the angular distribution of π^0 in x rest frame for $x \to \pi^0\pi^0$ (the polar angle θ (left) and the azimuthal angle ϕ (right)).

The best results can be achieved by fitting $\rho(1450)$, $f_2(1565)$ and $f_2(2300)$ in addition to $b_1(1235)$, $f_2(1270)$, σ and $f_0(980)$. Then, log-likelihood decreases to $\ln \mathcal{L} = 164012$.

The mass (in Figure 5.14) and the angular distributions (in Figure 5.15 and Figure 5.16) are in a better agreement with the data, the crosses are real data, yellow histogram is the fit function and red histogram is sidebins. .

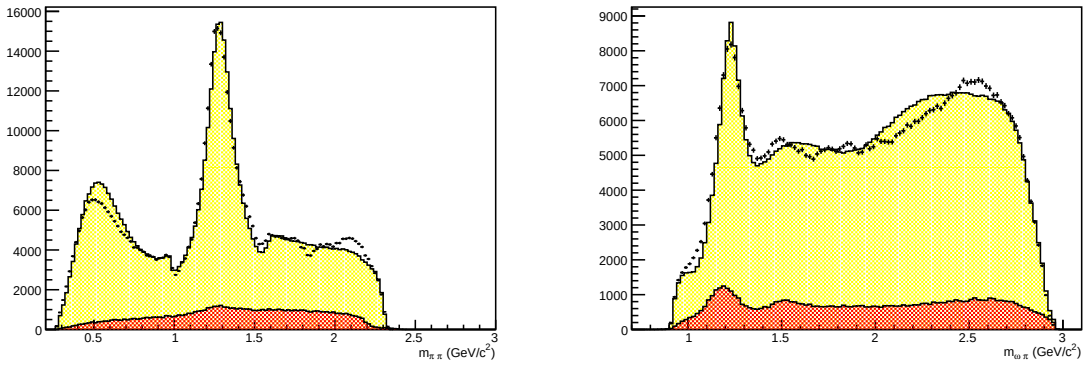

Figure 5.14. The invariant mass distuributions of pwa for $b_1(1235)$, $f_2(1270)$, $\rho(1450)$, $f_2(1565)$, $f_2(2300)$, σ and $f_0(980)$. the left histogram is the invariant mass distribution of $\pi^0\pi_0$, the right histogram is the invariant mass distribution of $\omega\pi_0$.

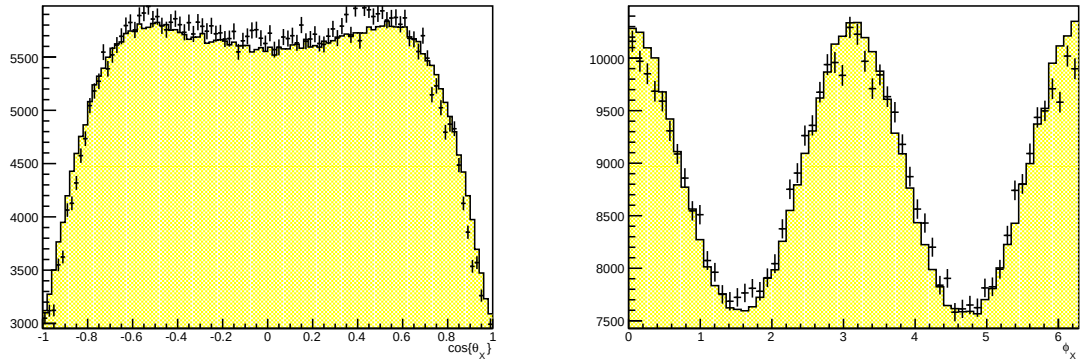

Figure 5.15. The production angular distributions of pwa for $b_1(1235)$, $f_2(1270)$, $\rho(1450)$, $f_2(1565)$, $f_2(2300)$, σ and $f_0(980)$. the angular distributions of x in j/ψ rest frame for $j/\psi \to \omega x$ (the polar angle θ (left) and the azimuthal angle ϕ (right)).

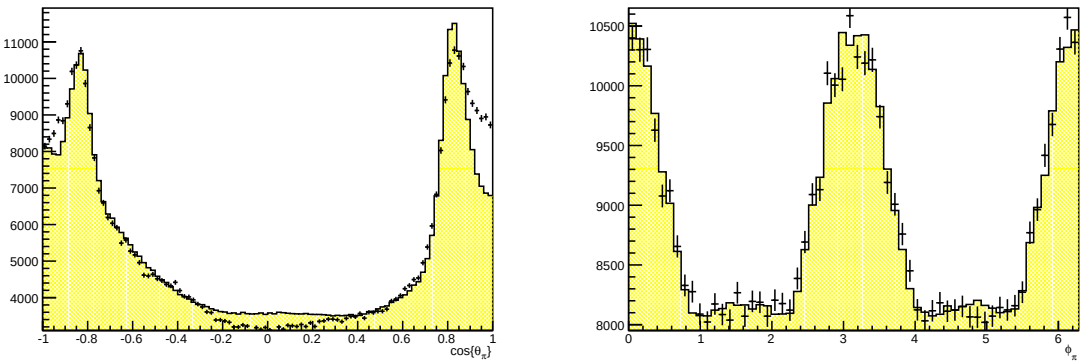

Figure 5.16. The decay angular distribution pwa for $b_1(1235)$, $f_2(1270)$, $\rho(1450)$, $f_2(1565)$, $f_2(2300)$, σ and $f_0(980)$. the angular distribution of π^0 in x rest frame for $x \to \pi^0\pi^0$ (the polar angle θ (left) and the azimuthal angle ϕ (right)).

In order to get the optima of masses and widths of fitted resonances we draw log-likelihood as a function of masses and widths. To localize visually the optima, the following graphes are drawn by setting the minimum log-likelihood to zero and drawing -$\Delta \ln \mathcal{L}$. Errors are statistical only and correspond to a change of 0.5 in log-likelihood.

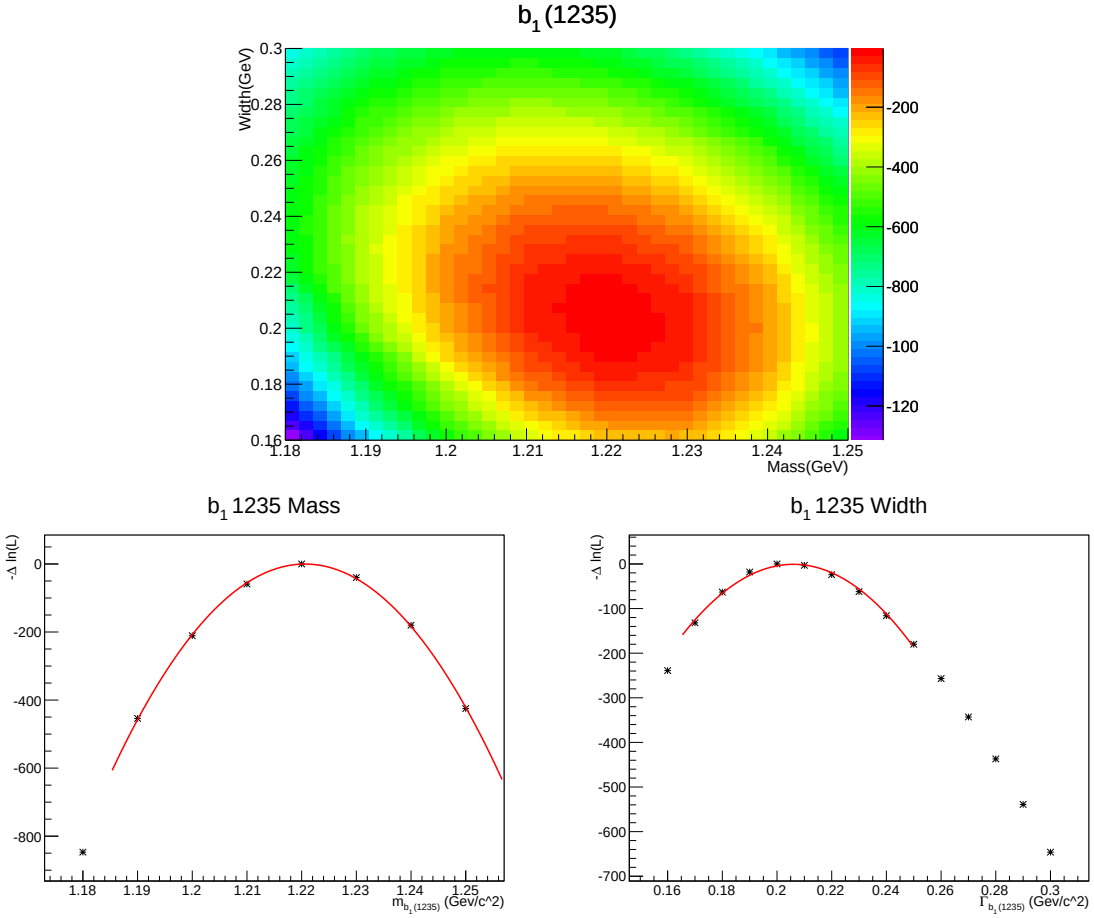

Figure 5.17. Log-likelihood as a function of the mass and the width of $b_1(1235)$.

The optimisation in Figure 5.17 gives $m_{b_1(1235)} = 1220.6 \pm 1.0\,\text{MeV}$ and $\Gamma_{b_1(1235)} = 206.0 \pm 2.3\,\text{MeV}$. These result are compatible with PDG values ($m_{b_1(1235)} = 1229.5 \pm 3.2\,\text{MeV}$ and $\Gamma_{b_1(1235)} = 142 \pm 9\,\text{MeV}$), despite the fact that these are the initial fits of very preliminary PWA [15].

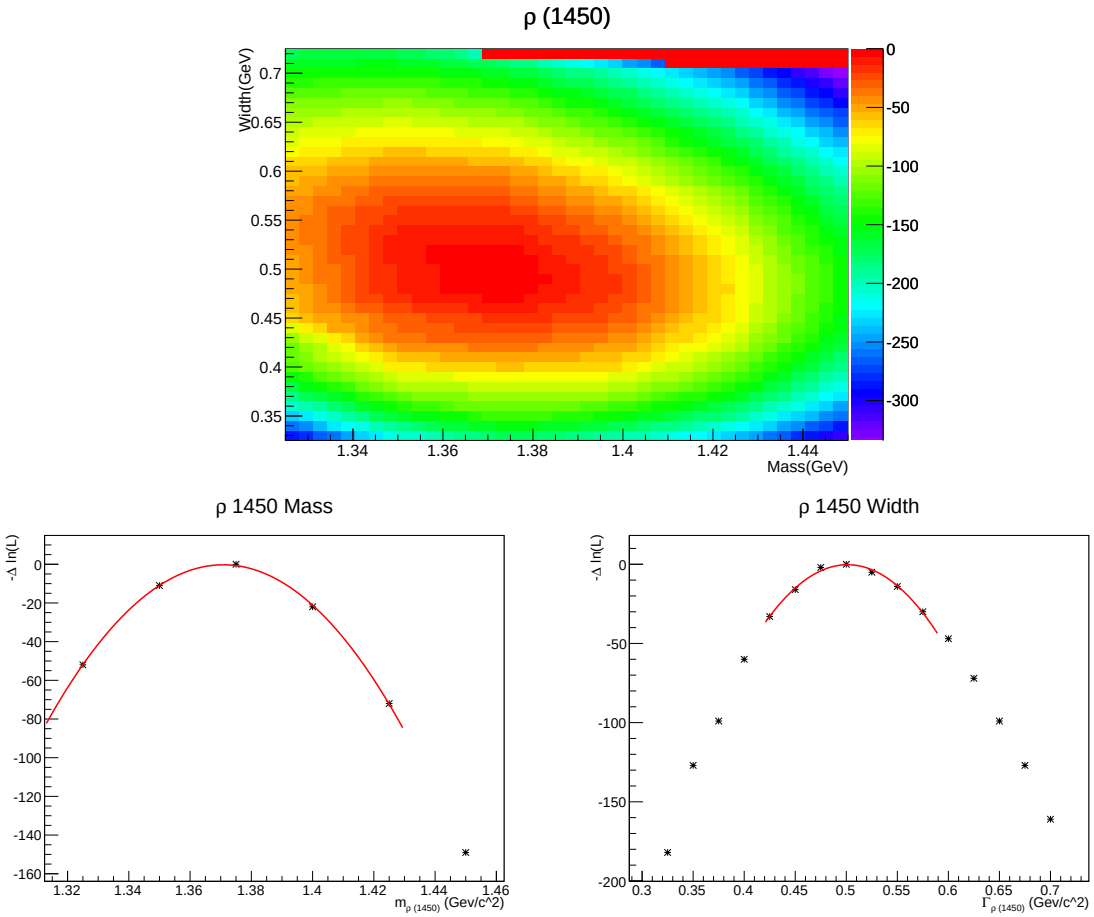

Figure 5.18. Log-likelihood as a function of the mass and the width of $\rho(1450)$.

The results of fits in Figure 5.18 are $m_{\rho(1450)} = 1370.8 \pm 4.5\,\text{MeV}$ and $\Gamma_{\rho(1450)} = 501.2 \pm 9.4\,\text{MeV}$. They are enough close to PDG values ($m_{\rho(1450)} = 1465 \pm 25\,\text{MeV}$ and $\Gamma_{\rho(1450)} = 400 \pm 60\,\text{MeV}$), taking in consideration that these are the initial fits of very preliminary PWA [15].

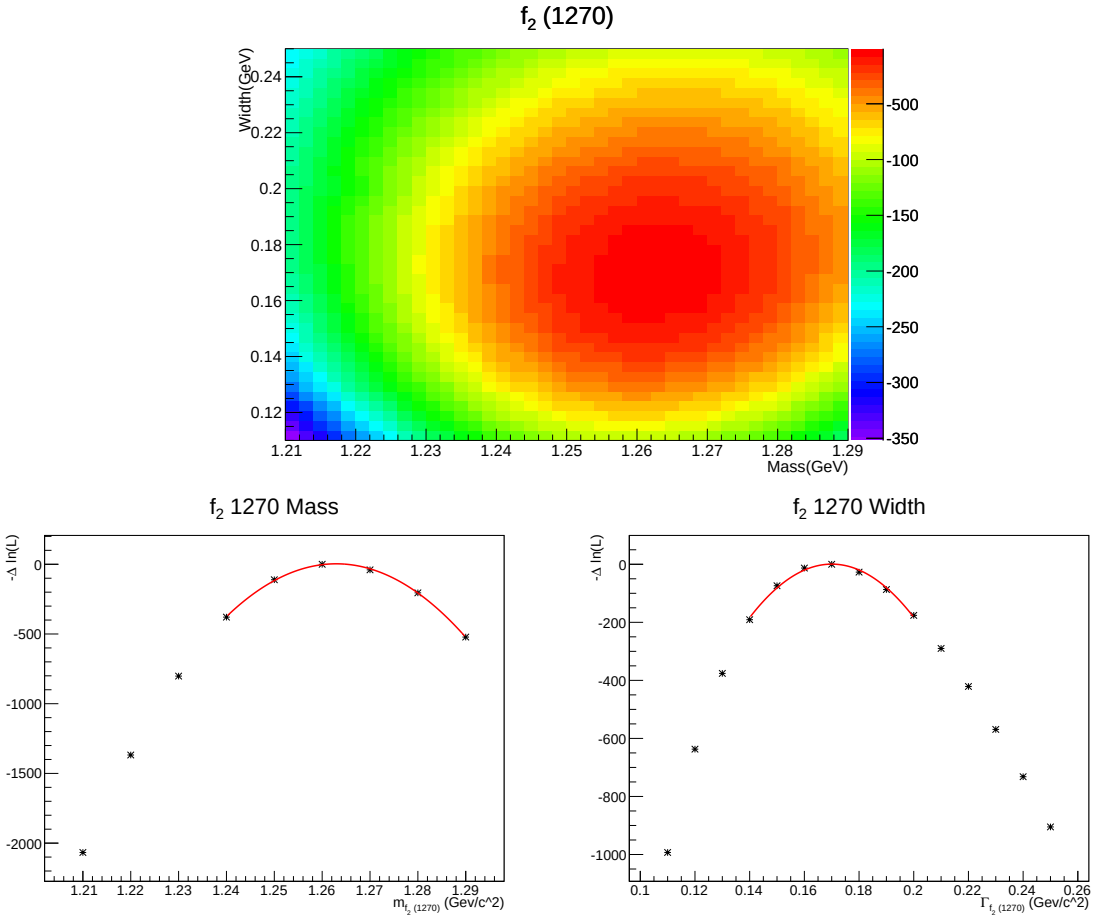

Figure 5.19. Log-likelihood as a function of the mass and the width of $f_2(1270)$.

The fits in Figure 5.19 give the result: $m_{f_2(1270)} = 1262.9 \pm 0.8\,\text{MeV}$ and $\Gamma_{f_2(1270)} = 170.0 \pm 1.6\,\text{MeV}$, which are consistant with PDG ($m_{f_2(1270)} = 1275.1 \pm 1.2\,\text{MeV}$ and $\Gamma_{f_2(1270)} = 184.2^{+4.0}_{-2.4}\,\text{MeV}$) [15].

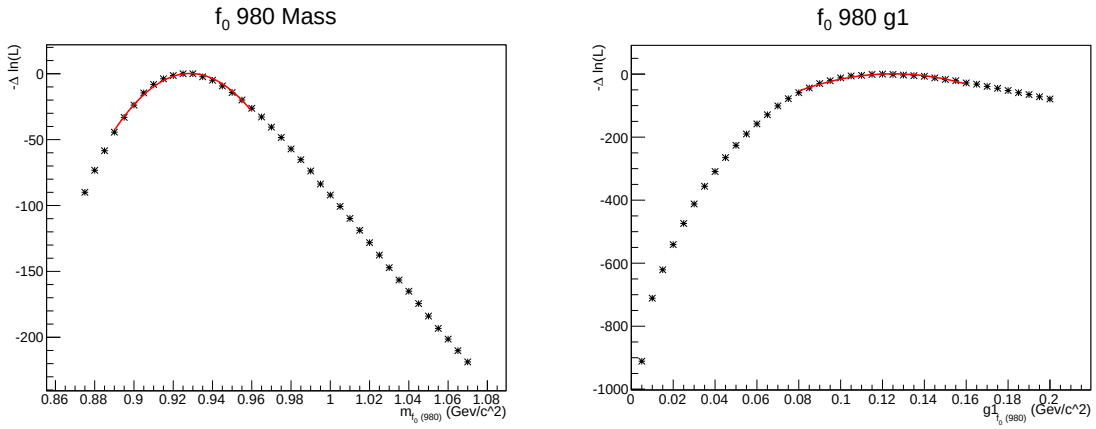

Figure 5.20. Log-likelihood as a function of the mass and $g_{\pi\pi}$ of $f_0(980)$.

Since Flatté formalism is used to fit $f_0(980)$, there are three variables to fit: mass, $g_{\pi\pi}$ and g_{KK}. In order to optimize all the three variables, a coupled analysis is needed: $J/\psi \to \omega\pi\pi$ and $J/\psi \to \omega K\bar{K}$. Since this analysis is for only $J/\psi \to \pi\pi$, the result of a former analysis at BESII, $g_{KK}/g_{\pi\pi} = 4.45$, is used [21, 27]. And fits gives the results for $f_0(980)$: $g_{\pi\pi} = 125.1 \pm 4.3\,\mathrm{MeV}$ and $m_{f_0(980)} = 928.6 \pm 4.1\,\mathrm{MeV}$, shown in Figure 5.20. This is consistant with the result of BESII ($m_{f_0(980)} = 970 \pm 7\,\mathrm{MeV}$ and $g_{\pi\pi} = 138 \pm 10\,\mathrm{MeV}$ [21]).

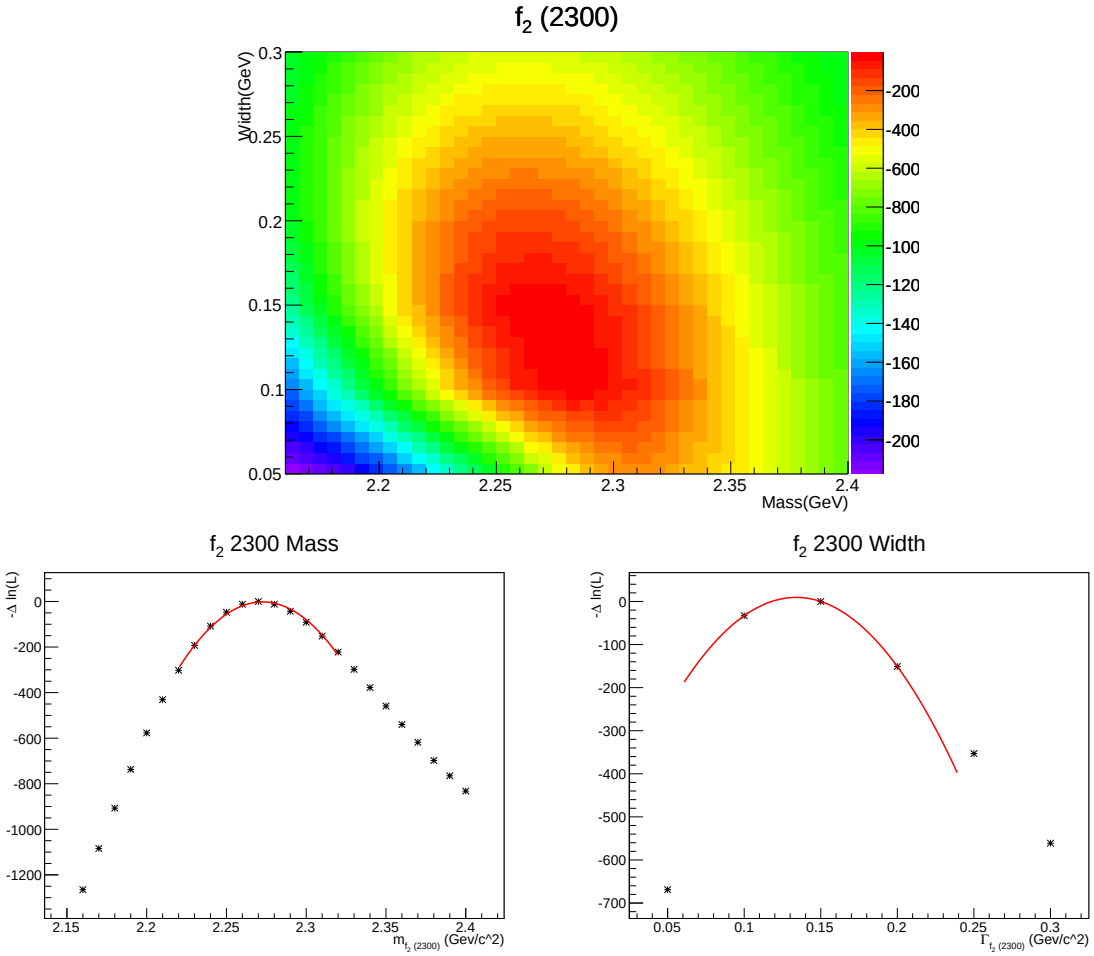

Figure 5.21. Log-likelihood as a function of the mass and the width of $f_2(2300)$.

The results of fits in Figure 5.21 are $m_{f_2(2300)} = 2272.7 \pm 2.2\,\text{MeV}$ and $\Gamma_{f_2(2300)} = 134.0 \pm 3.7\,\text{MeV}$. They are enough close to PDG values ($m_{f_2(2300)} = 2297 \pm 28\,\text{MeV}$ and $\Gamma_{f_2(2300)} = 149 \pm 41\,\text{MeV}$), taking in consideration that these are the initial fits of very preliminary PWA [15].

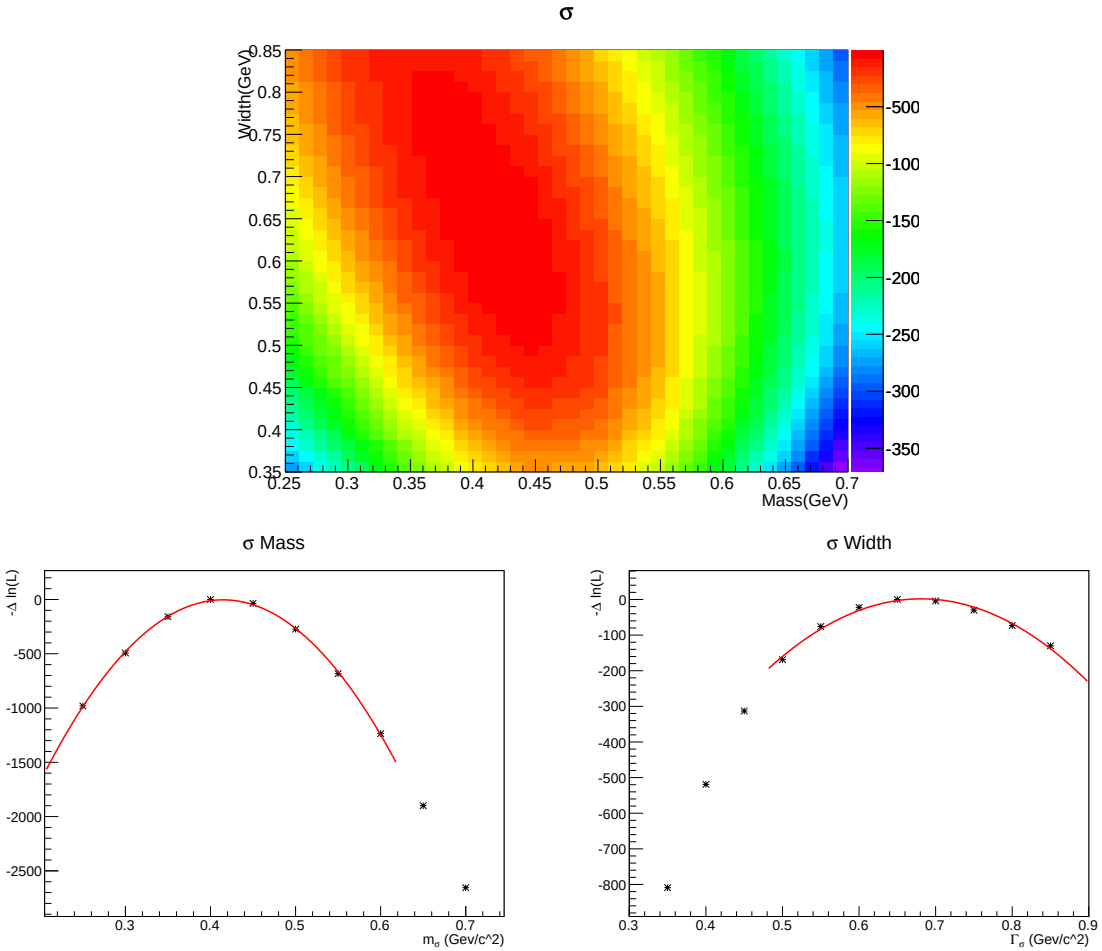

Figure 5.22. Log-likelihood as a function of the mass and the width of σ.

The results of fits in Figure 5.22 are $m_\sigma = 414.8 \pm 3.7\,\text{MeV}$ and $\Gamma_{\sigma=681.3\pm10.1}\,\text{MeV}$. They are enough close to results in BESII ($m_\sigma = 446^{+11+30}_{-9-32}$ and $\Gamma_\sigma = 578^{+36+114}_{-23-86}$) and consistent with PDG predictions ($m_\sigma = 400 - 550\,\text{MeV}$ and $\Gamma_\sigma = 400 - 700\,\text{MeV}$), taking in consideration that these are the initial fits of very preliminary PWA [15].

6. CONCLUSIONS

$J/\psi \to \omega\pi^0\pi^0$ has been studied, σ, $f_0(980)$, $f_2(1270)$, $b_1(1235)$ and $\rho(1450)$ particles have been observed, Dalitz Plot and sidebin analyses have been successfully performed. The results of the optimization of $f_2(1270)$, $b_1(1235)$ and $\rho(1450)$ are consistent with PDG. The measured mass and $g_{\pi\pi}$ of $f_0(980)$ are consistent with the earlier results of $J/\psi \to \omega\pi^+\pi^-$ from BESII experiment. The presence of $f_2(1565)$ in this channel is dubious. In the $J/\psi \to \omega\pi^+\pi^-$ analysis, it is claimed to be seen; however, it is not confirmed by this study.

A future re-optimization of all the parameters after including mass dependent widths in the Breit Wigner formula is likely to lead to better agreement with PDG. A very preliminary round of partial wave analysis (PWA) indicate that the channel purity and detector resolutions are well under control for this channel to be used for further detailed studies of various studies of the resonances in the $\omega\pi\pi$ system. Thanks to the high statistics it is possible to confirm the existence of resonances observed previously in the BESII data.

In conclusion, the very first study of the $J/\psi \to \omega\pi^0\pi^0$ channel at BESIII has been performed and the channel has been found to be promising, despite involving a rather complex final state with six photons and two pions. The signal-to-background ratio is high and the available statistics makes the channel attractive for future exploration of interesting resonances such as σ and $f_0(980)$.

APPENDIX A: Formulations

A.1. Relativistic Breit-Wigner Formula

Relativistic BW is a formalism to calculate amplitude of unstable resonances. It is the best formalism to describe isolated, non-overlapping resonances far from the threshold of additional decay channels [30].

$$f_{\mathrm{BW}} = \frac{1}{M^2 - s - iM\Gamma}$$

A.2. Flatté Formalism

Flstté formalism is developeed by Flatté in 1976 to explain unstable resonances near a threshold of an additional decay channel [26].

$$f_{\mathrm{Flatté}} = \frac{1}{M^2 - s - i\big(g_1\rho_1(s) + g_2 1\rho_2(s)\big)}$$

Especially for $a_0(980)$ and $f_0(980)$, which are very close to $K\bar{K}$ threshold, Flatté formulation is essential. For $a_0(980)$ (since a_0 usually decays to $\pi\eta$ [15]); $\rho_1 = \rho_{\pi\eta}$, $\rho_2 = \rho_{K\bar{K}}$, $g_1 = g_{\pi\eta}$ and $g_2 = g_{K\bar{K}}$. For $f_0(980)$ (since f_0 usually decays to $\pi\pi$ [15]); $\rho_1 = \rho_{\pi\pi}$, $\rho_2 = \rho_{K\bar{K}}$, $g_1 = g_{\pi\pi}$ and $g_2 = g_{K\bar{K}}$. Where $\rho = 2k/\sqrt{s}$ and k is the center of mass momentum of the π or K in the resonance rest frame [30].

APPENDIX B: Dalitz Plot

"I visualize geometry better than numbers."

— Richard Dalitz

Dalitz plot is a ternary plot, proposed by Richard H. Dalitz in his work about charged Kaons [38]. Dalitz plot is often used for three-body decays. However, it can be adopted to four particles [39]. Due to kinematic constraints a three-body decay can completely described by two variables (3 four-vectors have 12 degrees of freedom, but 4 constraints come from conservation of four momentum, 3 constraints come from masses of 3 particles and another 3 constraints come from Euler angles: $ndf = 12 - 4 - 3 - 3 = 2$). Usually, the squares of invariant masses of two pair of final products are used for Dalitz plot.

Let $A \to abc$, then the Dalitz plot will be m_{ab}^2 vs m_{bc}^2, where $m_{ij} = (E_i + E_i)^2 - (\vec{p_i} + \vec{p_j})^2$. If there is no angular correlation between decay products, plot will be flat; however, the symmetries would impose certain constraints and restrictions in the distribution. Furthermore, if there exists an intermediate particle -the mother particle decays into 2 particles and one of them decays into two again- the Dalitz plot will have a non-uniform distribution. By kinematic rules, we can optain:

$$m_{ab}^2 + m_{bc}^2 + m_{ac}^2 = W^2 + m_a^2 + m_b^2 + m_c^2 = C$$
$$m_{ac}^2 = C - m_{ab}^2 - m_{bc}^2$$

where W is center of mass energy of system and C is constant.

Thus, if there exists an intermediate resonance then Dalitz plot will have dense bands (or shallow bands in the case of destructive interference between resonances). For a resonance of $R \to ab$ there will be a horizontal band, for a resonance of $R \to bc$ there will be a vertical band and for resonance of $R \to ac$ there will be a diagonal band.

For a process $A \to abb$, Dalitz plot will be symmetric since Dalitz plot will be m_{ab} vs m_{ab}. Thus, resonances of $R \to bb$ will apear as both vertical and horizontal bands.

REFERENCES

1. Gell-Mann, M., "The interpretation of the New Particles as Displaced Charge Multiplets", *Il Nuovo Cimento*, Vol. 4, No. S2, pp. 848–866, 1956.

2. Gell-Mann, M., "A Schematic Model of Baryons and Mesons", *Physics Letters*, Vol. 8, No. 3, pp. 214 – 215, 1964.

3. Amsler, C. and N. A. Törnqvist, "Mesons Beyond the Naive Quark Model", *Physics Reports*, Vol. 389, No. 2, pp. 61–117, 2004.

4. Klempt, E. and A. Zaitsev, "Glueballs, hybrids, multiquarks: Experimental facts versus QCD inspired concepts", *Physics Reports*, Vol. 454, No. 1-4, pp. 1–202, 2007.

5. Jaffe, R. L., "Multiquark Hadrons", *Physical Review D*, Vol. 15, No. 1, pp. 267–289, 1977.

6. Wagner, M., C. Alexandrou, J. O. Daldrop, M. D. Brida, M. Gravina, L. Scorzato, C. Urbach and C. Wiese, "Scalar Mesons and Tetraquarks by Means of Lattice QCD", *PoS*, Vol. ConfinementX, p. 108, 2012.

7. Schumacher, M., "Observation of the Higgs Boson of Strong Interaction via Compton Scattering by the Nucleon", *The European Physical Journal*, Vol. C67, pp. 283–293, 2010.

8. Close, F. E. and N. A. Törnqvist, "Scalar Mesons Above and Below 1 GeV", *J. Phys.*, Vol. G28, pp. R249–R267, 2002.

9. BES Collaboration, "Observation of a Charged Charmoniumlike Structure in $e^+e^- \to \pi^+\pi^- J/\psi$ at $\sqrt{s}$ =4.26 GeV", *Physics Review Letters*, Vol. 110, p. 252001, 2013.

10. LHCb Collaboration, "Observation of $J/\psi p$ Resonances Consistent with Pentaquark States in $\Lambda_b^0 \to J/\psi K^- p$ Decays", , 2015, arXiv:1507.03414v1.

11. Glashow, S. L., "Partial-Symmetries of Weak Interaction", *Nuclear Physics*, Vol. 22, No. 4, pp. 579–588, 1961.

12. Weinberg, S., "A Model of Leptons", *Physical Review Letters*, Vol. 19, No. 21, pp. 1264–1266, 1967.

13. Salam, A., "Weak and Electromagnetic Interactions.", *Nobel Symposium 8*, 1968.

14. Higgs, P. W., "Broken Symmetries and the Masses of Gauge Bosons", *Physical Review Letters*, Vol. 13, No. 16, pp. 508–509, 1964.

15. PDG Collaboration, "Review of Particle Physics", *Chinese Physics*, Vol. C, No. 38, p. 090001, 2014.

16. Peskin, M. E., *An Introduction to Quantum Field Theory*, Perseus books publishing, 1995.

17. Weinstein, J. and N. Isgur, "$qqq\bar{q}q$ System in a Potential Model", *Physics Review D*, Vol. 27, No. 3, pp. 588–599, 1983.

18. Aubert, J. J., U. Becker, P. J. Biggs, J. Burger, M. Chen, G. Everhart, P. Goldhagen, J. Leong, T. McCorriston, T. G. Rhoades, M. Rohde, S. C. C. Ting, S. L. Wu and Y. Y. Lee, "Experimental Observation of a Heavy Particle J", *Physics Rewiew Letters*, Vol. 33, pp. 1404–1406, 1974.

19. SLAC Collaboration, "Discovery of a Narrow Resonance in e^+e^- Annihilation", *Physics Review Letters*, Vol. 33, pp. 1406–1408, Dec 1974.

20. "BESIII Experiment", `http://bes3.ihep.ac.cn`, 2015, [Accessed July-2015].

21. BES Collaboration, "The Sigma Pole in $J/\psi \to \omega\pi^+\pi^-$", *Physics Letters*, Vol. B,

No. 598, pp. 149–158, 2004.

22. De Min Li and Hong Yu and Qi-Xing Shen, "Properties of the Tensor Mesons $f_2(1270)$ and $f_2'(1525)$", *Journal of Physics G: Nuclear and Particle Physics*, Vol. 27, No. 4, p. 807, 2001.

23. Burakovsky, L. and L. P. Horwitz, "Hadronic Resonance Spectrum May Help in Resolution of Meson Nonet Enigmas", *Nuclear Physics*, Vol. A609, pp. 585–599, 1996.

24. Cheng, H. Y., "Hadronic D Decays Involving Scalar Mesons", *Physics Review D*, Vol. 67, No. 034024, 2003.

25. Anisovich, V. V. , "Systematics of Quark-Antiquark States and Scalar Exotic Mesons", *Physics-Uspekhi*, Vol. 47, No. 1, p. 45, 2004.

26. Flatté, S., "Coupled-Channel Analysis of the $\pi\eta$ and $K\bar{K}$ Systems Near $K\bar{K}$ Threshold", *Physics Letters B*, Vol. 63, No. 2, pp. 224 – 227, 1976.

27. BES Collaboration, "Study of $J/\psi \to \omega K^+K^-$", *Physics Letters*, Vol. B603, pp. 138–145, 2004.

28. Lee, H. J. and N. I. Kochelev, "Instanton Interpolating Current for σ-tetraquark", *Physics Letters*, Vol. B642, pp. 358–365, 2006.

29. "Introduction to IHEP", `http://www.ihep.ac.cn/english/ihep.htm`, 2015, [Accessed May-2015].

30. BES Collaboration, "Physics at BES-III", *International Journal of Modern Physics A*, Vol. 24, No. 1, 2009.

31. "Brief Introduction of Beijing Synchrotron Radiation Facility", `http://english.ihep.cas.cn/rs/fs/srl/aboutbsrf/briefintroduction/201204/t20120417\_83958.html`, 2015, [Accessed May-2015].

32. BES Collaboration, "Design and Construction of BESIII", *Nuclear Instruments and Methods in Physics*, Vol. A, No. 614, pp. 345–399, 2010.

33. BES Collaboration, "BES3 Time of Flight Monitoring System", *Nuclear Instruments and Methods in Physics*, Vol. A, No. 593, pp. 255–262, 2008.

34. Barrand, G., I. Belyaev, P. Binko, M. Cattaneo, R. Chytracek, G. Corti, M. Frank, G. Gracia, J. Harvey, E. van Herwijnen, P. Maley, P. Mato, S. Probst and F. Ranjard, "GAUDI - A software Architecture and Framework for Building HEP Data Processing Applications", *Computer Physics Communications*, , No. 140, pp. 45–55, 2001.

35. Geant4 Collaboration, "GEANT4 A Simulation Toolkit", *Nuclear Instruments and Methods in Physics*, Vol. A, No. 506, pp. 250–303, 2003.

36. Deng, Z. Y., G. F. Cao, C. D. Fu, M. He, H. M. Liu, Y. J. Mao, Y. Xia, Z. Y. You, Y. Yuan, R. Tang, Y. J. Liu, Q. M. Ma, X. Ma, D. Y. Wang, Z. P. Mao, S. P. Wen, Z. Wang, W. D. Li, C. C. Zhang, J. F. Qiu, X. Y. Zhang, X. M. Zhang, Y. Zhang, Z. Zheng, G. W. Yu, X. T. Huang, L. L. Jiang and S. Zang, "Object-Oriented BESIII Detector Simulation System", *High Energy Physics And Nuclear Physics*, , No. 30, pp. 371–377, 2006.

37. Ping, R. G., "Event Generators at BESIII", *Chinese Physics*, Vol. C, No. 32, pp. 599–602, 2008.

38. Dalitz, R. H., "On the Analysis of τ-Meson Data and the Nature of the τ-meson", *The London, Edinburgh, and Dublin Philosophical Magazine and Journal of Science*, Vol. 44, No. 357, pp. 1068–1080, 1953.

39. Schulz, M., D. Fischer, T. Ferger, R. Moshammer and J. Ullrich, "Four-Particle Dalitz Plots to Visualize Atomic Break-up Processes", *Journal of Physics B: Atomic, Molecular, and Optical Physics*, Vol. 40, No. 15, pp. 3091–3099, 2007.